1976

ELECTRIC-FIELD INDUCED QUANTUM BEATS OF METASTABLE HYDROGEN.

EE-HUA. GOH
University of Windsor

Recommended Citation

GOH, EE-HUA., "ELECTRIC-FIELD INDUCED QUANTUM BEATS OF METASTABLE HYDROGEN." (1976). *Electronic Theses and Dissertations*. 1895.
https://scholar.uwindsor.ca/etd/1895

ELECTRIC-FIELD INDUCED QUANTUM BEATS OF METASTABLE HYDROGEN

by

Ee-Hua Goh

A Dissertation
submitted to the Faculty of Graduate Studies
through the Department of
Physics in Partial Fulfillment
of the requirements for the Degree
of Doctor of Philosophy at
The University of Windsor

Windsor, Ontario, Canada

1976

ABSTRACT

Field-induced quantum beats observed in beam-foil studies of Lyman-α radiation are obtained in a conventional metastable hydrogen quenching experiments. A monoenergetic beam of metastable hydrogen atoms of velocities ~10^8cm/sec enters a static electric field perpendicular to the beam axis. The quenching cell consists of a parallel plate capacitor whose fringing field has been greatly reduced by means of a resistively coated end-plate. The field is in effect switched-on sufficiently fast to resolve the rapid fine structure oscillation (~10969MHz) in the beat pattern. The resultant radiation is observed in the direction parallel to the field since structure in this radiation is most pronounced. The results are in good agreement with the non-perturbative theory of Drake and Grimley, without the use of adjustable parameters for the initial state amplitudes. The present experiments are the first to separate quantitatively some of the hyperfine structure transitions between the $2S_{1/2}$ - $2P_{1/2}$ states and also between the $2S_{1/2}$ - $2P_{3/2}$ states.

ACKNOWLEDGEMENT

I would like to express my sincere thanks to Dr. A. van Wijngaarden under whose supervision and with whose invaluable assistance this research has been carried out, and for his corrections of this dissertation in manuscript.

I would also like to thank Dr. G.W.F. Drake for numerous discussions on the theoretical part of the work and Dr. W.E. Baylis for allowing me to include the two-state problem in this dissertation.

I am indebted to Professor P.S. Farago for being an active member of our research team during the summer of 1975 and for his guidance during the work.

Acknowledgement is due to Dr. J.W. McConkey for proof reading of the manuscipt.

TABLE OF CONTENTS

CHAPTER

LIST OF TABLES

LIST OF FIGURES

CHAPTER I

INTRODUCTION

Quantum beats or beat phenomena resulting from interference effects of atomic states have received much attention in the last two decades, particularly through studies in beam-foil spectroscopy (for a review, see Andrä, 1974). Here a fast beam of atomic particles is made to traverse a thin foil a few tens of nanometers thick. Because of the violent interaction between the beam particles and the foil practically any excited state of the projectile, regardless of its charge state, can be excited. Once a state is excited, it can be studied in flight with high time resolution of the order of 10^{-9} - 10^{-10} sec, by taking advantage of the high speed ($\sim 10^8$ cm/sec) of the beam particles. Another advantage of beam-foil spectroscopy is the very short excitation pulse of $\sim 10^{-14}$ sec, which will coherently excite the sublevels of a given state. Coherent excitation can usually occur when atoms experience a sudden change in their Hamiltonian. This fact can be understood if we consider two time regions; the atoms are in a well defined state described by the Hamiltonian H_2 at $t < 0$, and they enter a region in space where the Hamiltonian is H_1 at $t = 0$. If the transition is sudden, the excited state can be expanded in terms of a coherent superposition of eigenstates of H_1. Interference effects can be observed when components of the superposition state decay to a common ground state. The resulting oscillatory variations in the photon emission rate along the beam axis, downstream of the foil, are referred to as quantum beats. In beam-foil spectroscopy H_2 is the Hamiltonian in the foil and H_1 is the Hamiltonian for the emerging particles. If there is no field behind the foil H_1 is the field-free Hamiltonian and zero-field quantum beats can be observed. In the presence of an electric or magnetic field, H_1 includes field interactions.

In the experiments described in the present dissertation H_2 is the field-free Hamiltonian and H_1 is the Hamiltonian for a static electric field. The experiments are carried out with a beam of metastable hydrogen atoms H(2s) whose field free lifetime is very long (~0.14 sec). The beam travels at ground potential and is suddenly subjected to a static electric field. The external field, by mixing in the radiative 2p states, strongly decreases the effective lifetime and radiative transitions to the ground state take place with the emission of Lyman-α photons. The destruction of metastables by an external field is called quenching and the resulting radiation is called the quench radiation.

One of the great advantages of beam-foil spectroscopy is that the particles emerge from the foil in an initial non-statistical sublevel population, which is a requirement for the generation of quantum beats. The great disadvantage, however, is that these populations cannot be accurately predicted (Alguard and Drake, 1973; Andrä et al. 1973) and the initial state amplitudes are usually taken as adjustable parameters to fit the data. A precision experiment of the n=2 levels of hydrogen would in principle require $\sum_{\ell=0}^{1}(2\ell+1)(2s+1)(2I+1)=16$ adjustable parameters. Since this makes a comparison with theory somewhat arbitrary, Andrä (1974) studied n=2 Stark-beats for hydrogen without foil excitation. Coherent excitation was achieved by suddenly switching on a static electric field onto a clean beam of metastable hydrogen atoms in which the initial state amplitudes were known. In the experiment the beam passes through a small hole in the center of a metal plate, which is kept at ground potential and forms the first electrode of a parallel plate capacitor. The beam then travels parallel to the direction of the applied electric field and leaves the field through a hole in the second plate. Because of the geometry Andrä was only able to study the quench radiation emitted perpendicular to the field direction. Although Andrä observed a strong beat pattern at the Stark-shifted $2S_{1/2}$-$2P_{1/2}$ Lamb-shift frequency, no numerical results were reported. Furthermore our calculations (Section II.4) show that the quench radiation emitted parallel to the field direction contains much more information than the perpendicular intensity.

In addition to the Stark-shifted Lamb-shift frequency the intensity should also exhibit fine structure beats at much higher frequency corresponding to the $2P_{3/2}$-$2S_{1/2}$ and $2P_{3/2}$- $2P_{1/2}$ fine structure splittings. The $2P_{3/2}$-$2P_{1/2}$ fine structure beats have been observed (Andrä et al. 1973) in a motional electric field, $\vec{F}=\vec{v}\times\vec{B}/c$, after beam-foil excitation.

The experiments have not been precise enough to resolve these oscillations from the $2P_{3/2} - 2S_{1/2}$ beat. The disadvantage of a motional electric field rather than a static electric field is that it involves additional complications arising from Zeeman splitting.

In our experiment the beat pattern for metastable hydrogen is studied with a static electric field and with high spatial resolution along the beam axis. The quenching theory is described in Chapter II. The novel way (see Chapter III) in which the quenching field is applied transverse to the beam direction has enabled us to observe the quench radiation parallel to the electric field direction. The oscillations in the beat pattern of this radiation (Chapter IV) are sufficiently strong that a Fourier analysis (Chapter V) has resolved several transitions amongst the hyperfine structure states in the n=2 system of hydrogen.

CHAPTER II

THEORY

II.1 The n=2 System for Hydrogen

The various hyperfine structure states for the n=2 system of hydrogen are shown in Fig. 1. The levels lie about 10.2eV above the $1S_{1/2}$ ground state. The degeneracy between the $2P_{1/2}$ and $2P_{3/2}$ states is removed by the relativistic variation of electronic mass with velocity and by the spin-orbit coupling. Although Dirac predicted an exact degeneracy for the $2S_{1/2}$ and $2P_{1/2}$ states, Lamb and Retherford (1947) found a small energy difference of 1058MHz between these states. This so-called Lamb shift arises from quantum electrodynamical effects. Experimental values (Lundeen and Pinkin, 1975; Robiscoe and Shyn, 1970) with six significant figures are in good agreement with theory (Erickson, 1971; Mohr, 1975).

The average value of the measured energy difference between the $2P_{3/2}$ and $2S_{1/2}$ state is 9911MHz (Kaufman et al. 1971; Shyn et al. 1971; Cosens and Vorburger, 1970). When this value is combined with the Lamb shift measurement the fine structure splitting of the 2P state becomes 10969MHz, which is in good agreement with the calculated value of 10969.0542MHz (Brodsky and Parsons, 1967).

Since the nuclear spin of the hydrogen atom is I=1/2, the $2S_{1/2}$, $2P_{1/2}$ and $2P_{3/2}$ states consist of four, four and eight hyperfine substates, respectively. The measured value

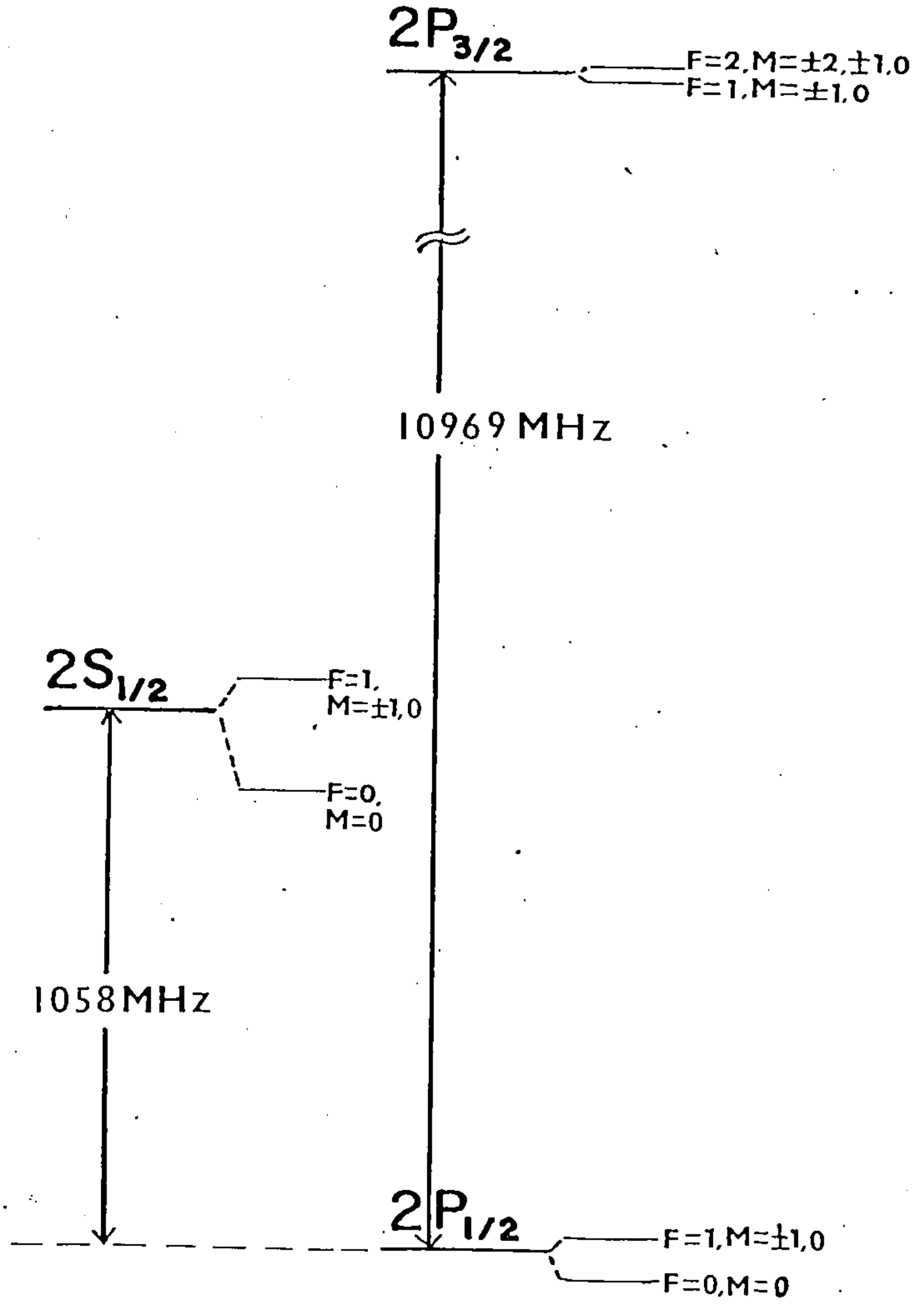

Fig. 1 Energy-level diagram for the n = 2 system of hydrogen.

of the hyperfine splitting of the $2S_{1/2}$ states is 177MHz (Heberle et al. 1956) and that of $2P_{1/2}$ state is 59MHz (Lundeen et al. 1975).

Both the metastable ($2S_{1/2}$) and the ground state ($1S_{1/2}$) of hydrogen are of even parity and accordingly transitions between these states are dipole forbidden. However, the electron can decay to the ground state via the emission of two photons (Drake et al. 1969). Since this is a very unlikely process, the field free lifetime of the $2S_{1/2}$ state is 0.14 sec. This extraordinary large value can be exploited to obtain a neutral beam of hydrogen with the $2S_{1/2}$ state as the only excited state.

The interaction of metastable hydrogen with an external field results in the mixing of the sixteen n=2 substates (the four 2S states and the twelve 2P states). Since the lifetime of the 2P states is very short (~1.6 nsec) radiative transition with the emission of Lyman-α photons (~121.6 nm) to the $1S_{1/2}$ ground state take place. When the external field is switched on suddenly, the decay rate has an oscillating behavior with various beat frequencies. The field dependence of the quenching rate is described in Section II.4. In the next section we describe how electric-field induced beats arise for a simple two state system consisting of a single metastable 2S level and a single radiative 2P level.

II.2 Two-state Problem

The time evolution of an initial pure state after an electric field is suddenly switched on can be solved in closed form (Baylis) for a system of two states. The Hamiltonian can be denoted by

$$H=\begin{cases} H_o, & t<o \\ H_o + ezF, & t>o \end{cases} \tag{2.1}$$

where $F\hat{z}$ is the electric field and H_o is the field-free Hamiltonian. Let $|s\rangle$ and $|p_z\rangle$ be the eigenstates of the system with corresponding eigenvalues $E_s = E_s^o$ and $E_p = E_p^o - i\Gamma_p/2$, for $t<o$. Γ_p is the level width for the $|p_z\rangle$ state. The eigenstates for $t>o$ can be represented by

$$|\pm\rangle = |s\rangle \; A_\pm + |p_z\rangle \; B_\pm \; . \tag{2.2}$$

The corresponding eigenvalues $\hbar\Omega_\pm - i\Gamma_\pm/2$ satisfy

$$H(t>o) \; |\pm\rangle = (\hbar\Omega_\pm - i\Gamma_\pm/2)|\pm\rangle \tag{2.3}$$

which, in matrix notation becomes

$$\begin{pmatrix} E_s & FV_{sp} \\ FV_{ps} & E_p \end{pmatrix} \begin{pmatrix} A_\pm \\ B_\pm \end{pmatrix} = (\hbar\Omega_\pm - i\Gamma_\pm/2) \begin{pmatrix} A_\pm \\ B_\pm \end{pmatrix} \tag{2.4}$$

where $$V_{ps} = V_{sp} = \langle s|ez|p\rangle \; .$$

Thus $\hbar\Omega_\pm - i\Gamma_\pm/2$ are given by the roots $\beta_\pm$ of the secular equation

$$\beta^2 - (E_s+E_p)\beta + E_sE_p - F^2V_{sp}^2 = 0 \tag{2.5}$$

or

$$\beta_\pm = \hbar\Omega_\pm - i\Gamma_\pm/2$$

$$= \{E_s^o + E_p^o - i\Gamma_p/2 \pm \sqrt{(E_s^o - E_p^o + i\Gamma_p/2)^2 + 4F^2V_{sp}^2}\}/2. \tag{2.6}$$

From (2.4), it follows that

$$E_s A_\pm + FV_{sp} B_\pm = (\hbar\Omega_\pm - i\Gamma_\pm/2)A_\pm$$

which yields

$$\alpha_\pm = B_\pm/A_\pm$$

$$= \{-E_s + (\hbar\Omega_\pm - i\Gamma_\pm/2)\}/FV_{sp}. \tag{2.7}$$

From (2.5) and (2.7) one obtains

$$\alpha_+ \alpha_- = -1. \tag{2.8}$$

The normalization condition $\langle + | + \rangle = \langle - | - \rangle = 1$ gives

$$|A_\pm|^2 + |B_\pm|^2 = 1$$

which can be written as

$$|A_\pm| = (1 + |\alpha_\pm|^2)^{-1/2} \tag{2.9}$$

Substitution of (2.9) into (2.2) and using the definition of $\alpha_\pm$ yields

$$|\pm\rangle = (1+|\alpha_\pm|^2)^{-1/2} (|s\rangle + |p_z\rangle \alpha_\pm). \tag{2.10}$$

The general non-stationary state can be written as a linear combination of $|\pm\rangle$,

$$|t\rangle = c_+ |+\rangle e^{-i\Omega_+ t - \Gamma_+ t/2\hbar} + c_- |-\rangle e^{-i\Omega_- t - \Gamma_- t/2\hbar}. \tag{2.11}$$

If the system consists of a pure state initially,

$$|t=0\rangle = |s\rangle \ . \tag{2.12}$$

Using (2.10) and (2.11),(2.12)becomes

$$\left(\frac{c_+}{\sqrt{1+|\alpha_+|^2}}+\frac{c_-}{\sqrt{1+|\alpha_-|^2}}\right)|s\rangle+\left(\frac{c_+\alpha_+}{\sqrt{1+|\alpha_+|^2}}+\frac{c_-\alpha_-}{\sqrt{1+|\alpha_-|^2}}\right)|p_z\rangle=|s\rangle \ . \tag{2.13}$$

The values of $c_\pm$ are then given by

$$\begin{cases} \dfrac{c_+}{\sqrt{1+|\alpha_+|^2}}+\dfrac{c_-}{\sqrt{1+|\alpha_-|^2}}=1 \\ \dfrac{c_+\alpha_+}{\sqrt{1+|\alpha_+|^2}}+\dfrac{c_-\alpha_-}{\sqrt{1+|\alpha_-|^2}}=0 \end{cases} \tag{2.14}$$

The solution of Equations (2.14) gives

$$c_\pm = \frac{\alpha_\mp\sqrt{1+|\alpha_\pm|^2}}{\alpha_\mp - \alpha_\pm} \tag{2.15}$$

Substitution of (2.15) into (2.11), using (2.8), yields

$$|t\rangle=\frac{1}{\alpha_--\alpha_+}\{|s\rangle(\alpha_- e^{-i\Omega_+t-\Gamma_+t/2\hbar}-\alpha_+e^{-i\Omega_-t-\Gamma_-t/2\hbar}) -|p_z\rangle(e^{-i\Omega_+t-\Gamma_+t/2\hbar}-e^{-i\Omega_-t-\Gamma_-t/2\hbar})\}. \tag{2.16}$$

If the $|s\rangle$ state is metastable and the system only radiates from the $|p_z\rangle$ state, then the emission rate is proportional to the probability of finding the system in the $|p_z\rangle$ state. This probability is

$$|\langle p_z|t\rangle|^2 = \frac{1}{|\alpha_+-\alpha_-|^2}\left|e^{-i\Omega_+t-\Gamma_+t/2\hbar} - e^{-i\Omega_-t-\Gamma_-t/2\hbar}\right|^2 \quad . \qquad (2.17)$$

Substitution of (2.6) gives

$$|\langle p_z|t\rangle|^2 = \frac{F^2V_{sp}^2}{(E_s-E_p)^2+4F^2V_{sp}^2}\{e^{-\Gamma_+t/\hbar} + e^{-\Gamma_-t/\hbar}$$

$$-2e^{-(\Gamma_++\Gamma_-)t/2\hbar}\cos(\Omega_+-\Omega_-)t\} \qquad (2.18)$$

where, from (2.6),

$$\Omega_\pm = (E_s^o + E_p^o \pm g_+)/2\hbar \qquad (2.19)$$

$$\Gamma_\pm = \Gamma_p/2 \mp g_- \qquad (2.20)$$

with g_+ and g_- given by

$$g_+ + i\,g_- = \sqrt{(E_s^o - E_p^o + i\Gamma_p/2)^2 + 4F^2V_{sp}^2}$$

or, to be more explicit,

$$g_\pm = \sqrt{\left\{\sqrt{f^2 + (E_s^o - E_p^o)^2\Gamma_p^2} \pm f\right\}/2} \qquad (2.21)$$

where

$$f = (E_s^o - E_p^o)^2 - \Gamma_p^2/4 + 4F^2V_{sp}^2 \quad . \qquad (2.22)$$

It can be seen from (2.18) that an oscillatory behavior is superimposed on the exponential decay with an angular frequency $\Omega_+ - \Omega_-$ equal to the energy difference between the Stark-shifted states (cf. Eq. 2.3).

An intuitive interpretation for quantum beat phenomena can now be obtained as follows. From (2.18) it can be seen that the probability of finding the system in the radiative $|p_z\rangle$ state oscillates in time. It is obvious that $|\langle s|t\rangle|^2$ oscillates with the same frequency. Whenever the probability for the system to be in the $|s\rangle$ state is large, the probability of it to be in the $|p_z\rangle$ state is small and vice versa. Since the radiative decay rate from the $|s\rangle$ state vanishes and that from the $|p_z\rangle$ state is high, the intensity of light emission will be modulated with a frequency precisely equal to that of the transition probability.

An exact treatment of the quenching process for H(2s) that takes the sixteen n=2 states into account is described in the next two sections. Even though the quench radiation contains several beat frequencies, the intuitive picture developed above will still be valid.

II.3 Non-perturbative Theory

In this section the non-perturbative theory of Drake and Grimley(1975), applied to the n=2 system of hydrogen atom, is summarized.

The time-dependent Schrödinger equation is

$$i\hbar\frac{\partial}{\partial t}\Psi(\vec{r},t) = \{ H_0 + V(\vec{r},t) \}\Psi(\vec{r},t) \qquad (2.23)$$

Where H_o is the field-free atomic Hamiltonian, including the fine structure and the hyperfine structure interactions. The field-free states Ψ_n satisfy the eigenequation

$$H_o\Psi_n = E_n^o \Psi_n \quad . \tag{2.24}$$

The level width Γ_n corresponding to the energy level E_n^o is introduced phenomenologically by

$$E_n = E_n^o - i\Gamma_n/2 \ . \tag{2.25}$$

The interaction potential due to the external field is represented by

$$V(\vec{r},t) = \begin{cases} FV(\vec{r})e^{-\varepsilon t} & , \quad t>0 \\ 0 & , \quad t<0 \end{cases} \tag{2.26}$$

where F is the field strength and ε is any complex number with a positive real part.

The evolution of the state is given by

$$\theta(t_1-t_2)\Psi_n(\vec{r}_1,t_1)=\hbar\int G^+(1;2)\Psi_n(\vec{r}_2,t_2)d\vec{r}_2 \tag{2.27}$$

where, for $t_2<0$,

$$\Psi_n(\vec{r}_2,t_2) = \Psi_n(\vec{r}_2)e^{-iE_nt_2/\hbar} \tag{2.28}$$

is one of the field-free states and $\theta(t_1-t_2)$ is the unit step function.

Drake and Grimley(1975) show that for $t_2<0$, $t_1>0$ the retarded Green's function can be written in the form

$$G^{+}(1;2) = \frac{1}{2\pi i}\int_{-\infty}^{\infty} d\omega_1 \; e^{i\omega_1 t_1} \underset{\sim}{\Psi}^{+}(\vec{r}_2,t_2)\underset{\sim}{g}(\omega_1)\underset{\sim}{\Psi}(\vec{r}_1) \quad . \qquad (2.29)$$

where $\underset{\sim}{\Psi}(\vec{r}_1)$ is a column vector of eigenstates $\Psi_n(\vec{r}_1)$ and $\underset{\sim}{\Psi}^{+}(\vec{r}_2,t_2)$ is the Hermitian conjugate row vector of states $\Psi_n(\vec{r}_2)e^{-iE_n t_2/\hbar}$. The square matrix function $\underset{\sim}{g}(\omega_1)$ is the particular solution to the differential equation

$$\{\underset{\sim}{\Delta}(\omega_1) - \underset{\sim}{1}i\varepsilon F\frac{d}{dF} + F\underset{\sim}{V}^{+}\}\; \underset{\sim}{g}(\omega_1,F) = \underset{\sim}{1} \qquad (2.30)$$

where $\underset{\sim}{\Delta}(\omega_1)$ is a square diagonal matrix with diagonal elements $\Delta_n = E_n + h\omega_1$ and $\underset{\sim}{V}$ is the interaction matrix with elements

$$V_{mn} = \langle \Psi_m(\vec{r}) \mid V(\vec{r}) \mid \Psi_n(\vec{r}) \rangle \quad . \qquad (2.31)$$

In the limit $F\to 0$, the solution to (2.30) is

$$\underset{\sim}{g}_o(\omega_1) = \underset{\sim}{\Delta}^{-1}(\omega_1) \quad . \qquad (2.32)$$

Substitution of the previous expression into (2.29) gives the free-particle propagator

$$G_o^{+}(1;2) = \frac{1}{2\pi i}\int_{-\infty}^{\infty} d\omega_1 e^{i\omega_1 t_1} \sum_n \frac{\Psi_n(r_1)\Psi_n^{*}(r_2)}{E_n + \hbar\omega_1} e^{iE_n t_2/\hbar} \quad . \qquad (2.33)$$

In the limit $\varepsilon\to 0$, the solution for finite field strength is

$$\underset{\sim}{g}(\omega_1,\tilde{F}) = \{\; \underset{\sim}{\Delta}(\omega_1) + F\underset{\sim}{V}^{+} \;\}^{-1} \quad . \qquad (2.34)$$

In the electric dipole approximation, the interaction matrix $\underset{\sim}{V}$ has the off-diagonal structure

$$\underset{\sim}{V} = \begin{pmatrix} 0 & \underset{\sim}{V}_{sp} \\ \underset{\sim}{V}_{ps} & 0 \end{pmatrix} \qquad (2.35)$$

in the subspace containing N_s s-states and N_p p-states. Thus $\underset{\sim}{g}$ is the inverse of the matrix

$$\begin{pmatrix} \underset{\sim}{\Delta}_{ss} & F\underset{\sim}{V}_{sp} \\ F\underset{\sim}{V}_{ps} & \underset{\sim}{\Delta}_{pp} \end{pmatrix}$$

where $\underset{\sim}{\Delta}_{ss}$ and $\underset{\sim}{\Delta}_{pp}$ are the diagonal submatrices of $\underset{\sim}{\Delta}(\omega_1)$.

The inversion of the previous matrix gives

$$\underset{\sim}{g} = \begin{pmatrix} \underset{\sim}{D}_{ss}^{-1} & -F\underset{\sim}{D}_{ss}^{-1}\underset{\sim}{V}_{sp}\underset{\sim}{\Delta}_{pp}^{-1} \\ -F\underset{\sim}{D}_{pp}^{-1}\underset{\sim}{V}_{ps}\underset{\sim}{\Delta}_{ss}^{-1} & \underset{\sim}{D}_{pp}^{-1} \end{pmatrix} \qquad (2.36)$$

where

$$\underset{\sim}{D}_{ss} = \underset{\sim}{\Delta}_{ss} - F^2\underset{\sim}{V}_{sp}\underset{\sim}{\Delta}_{pp}^{-1}\underset{\sim}{V}_{ps} \qquad (2.37)$$

and

$$\underset{\sim}{D}_{pp} = \underset{\sim}{\Delta}_{pp} - F^2\underset{\sim}{V}_{ps}\underset{\sim}{\Delta}_{ss}^{-1}\underset{\sim}{V}_{sp} \quad . \qquad (2.38)$$

The evaluation of

$$\underset{\sim}{g}_{sp} = -F\underset{\sim}{D}_{ss}^{-1}\underset{\sim}{V}_{sp}\underset{\sim}{\Delta}_{pp}^{-1} \qquad (2.39)$$

is thus reduced to the inversion of $N_s \times N_s$ matrix $\underset{\sim}{D}_{ss}$.

For the simple case where there is only one s-state and one p-state involved,

$$\underset{\sim}{g}(\omega_1) = \frac{1}{\Delta_{ss}\Delta_{pp} - F^2V_{sp}V_{ps}} \begin{pmatrix} \Delta_{pp} & -FV_{sp} \\ -FV_{ps} & \Delta_{ss} \end{pmatrix} .$$

If $\beta_1/\hbar$ and $\beta_2/\hbar$ are the roots of the equation

$$(E_s + \hbar\omega_1)(E_p + \hbar\omega_1) - F^2V_{sp}V_{ps} = 0 .$$

or,

$$\beta_1, \beta_2 = \frac{-E_s - E_p \mp \{(E_s - E_p)^2 + 4F^2V_{sp}V_{ps}\}^{1/2}}{2}$$

then

$$\underset{\sim}{g}(\omega_1) = \frac{1}{(\hbar\omega_1 - \beta_1)(\hbar\omega_1 - \beta_2)} \begin{pmatrix} E_p + \hbar\omega_1 & -FV_{sp} \\ -FV_{ps} & E_s + \hbar\omega_1 \end{pmatrix} .$$

The Fourier transform of $\underset{\sim}{g}(\omega_1)$ is

$$\underset{\sim}{g}(t_1) = \frac{1}{2\pi i}\int_{-\infty}^{\infty} d\omega_1 \; e^{i\omega t_1} \underset{\sim}{g}(\omega_1)$$

$$= \frac{1}{\beta_1 - \beta_2}\left\{\begin{matrix} (E_p+\beta_1)e^{i\beta_1 t_1/\hbar} - (E_p+\beta_2)e^{i\beta_2 t_1/\hbar} & -FV_{sp}(e^{i\beta_1 t_1/\hbar} - e^{i\beta_2 t_1/\hbar}) . \\ -FV_{ps}(e^{i\beta_1 t_1/\hbar} - e^{i\beta_2 t_1/\hbar}) & (E_s+\beta_1)e^{i\beta_1 t_1/\hbar} - (E_s+\beta_2)e^{i\beta_2 t_1/\hbar} \end{matrix}\right]$$

The retarded Green's function is

$$G^{+}(1;2) = \begin{pmatrix}\psi_s^{*}(\vec{r}_2,t_2) & \psi_p^{*}(\vec{r}_2,t_2)\end{pmatrix} \underset{\sim}{g}(t_1) \begin{pmatrix}\psi_s(\vec{r}_1)\\ \psi_p(\vec{r}_1)\end{pmatrix} .$$

If the initial state at $t_2=0$ is a pure s-state, then

$$\psi(\vec{r}_1,t_1) = \int G^{+}(1;2)\,\psi_s(\vec{r}_2)\, e^{-iE_s t_2/\hbar}\, d\vec{r}_2$$

$$= \frac{1}{\beta_1-\beta_2}\Big[\{(E_p+\beta_1)e^{i\beta_1 t_1/\hbar} - (E_p+\beta_2)e^{i\beta_2 t_1/\hbar}\}\psi_s(\vec{r}_1)$$

$$-FV_{sp}(e^{i\beta_1 t_1/\hbar} - e^{i\beta_2 t_1/\hbar})\psi_p(\vec{r}_1)\Big]$$

which is identical to $|t\rangle$ in (2.16) by replacing β_1 and β_2 in the previous expression by $-\beta_+$ and $-\beta_-$ respectively.

For the general case, choose the z-axis to lie along the direction of the electric field. $\underset{\sim}{D}_{ss}$ is then block diagonalized according to the magetic quantum number M_F where $\vec{F} = \vec{I} + \vec{J}$ is the total angular momentum. For the case of metastable hydrogen, I = 1/2, J = 1/2 ; hence F = 0 , 1. With μ and ν denoting the state $2S_{1/2}(F = 0,\ M_F = 0)$ and $2S_{1/2}(F = 1,\ M_F = 0)$ respectively, $\underset{\sim}{D}_{ss}^{-1}$ can be written as

$$\underset{\sim}{D}_{ss} = \begin{pmatrix} \underset{\sim}{d}^{(0)} & 0 & 0 \\ 0 & \underset{\sim}{d}^{(1)} & 0 \\ 0 & 0 & \underset{\sim}{d}^{(-1)} \end{pmatrix} \qquad (2.40)$$

where $\underset{\sim}{d}^{(\pm 1)}$ are 1×1 matrices given by

$$\underset{\sim}{d}^{(m)} = \frac{\det(\underset{\sim}{\Delta}_{pp}^{(m)})}{\prod_k \hbar(-\beta_k^{(m)}+\omega_1)} , \qquad m=\pm 1 \tag{2.41}$$

and $\underset{\sim}{d}^{(0)}$ is a 2×2 matrix with the elements given by

$$\underset{\sim}{d}^{(0)}_{\mu\mu} = \frac{\det(\underset{\sim}{\Delta}_{pp}^{(0)})}{\prod_k \hbar(-\beta_k^{(0)}+\omega_1)} \left(\Delta_\nu - F^2 \sum_n \frac{V_{\nu n} V_{n\nu}}{\Delta_{np}} \right) \tag{2.42}$$

$$\underset{\sim}{d}^{(0)}_{\nu\nu} = \frac{\det(\underset{\sim}{\Delta}_{pp}^{(0)})}{\prod_k \hbar(-\beta_k^{(0)}+\omega_1)} \left(\Delta_\mu - F^2 \sum_n \frac{V_{\mu n} V_{n\mu}}{\Delta_{np}} \right) \tag{2.43}$$

$$\underset{\sim}{d}^{(0)}_{\mu\nu} = \frac{\det(\underset{\sim}{\Delta}_{pp}^{(0)})}{\prod_k \hbar(-\beta_k^{(0)}+\omega_1)} \left(F^2 \sum_n \frac{V_{\mu n} V_{n\nu}}{\Delta_{np}} \right) \tag{2.44}$$

and

$$\underset{\sim}{d}^{(0)}_{\nu\mu} = \frac{\det(\underset{\sim}{\Delta}_{pp}^{(0)})}{\prod_k \hbar(-\beta_k^{(0)}+\omega_1)} \left(F^2 \sum_n \frac{V_{\nu n} V_{n\mu}}{\Delta_{np}} \right) . \tag{2.45}$$

In the above expressions $\beta^{(m)}$ is the negative of the eigenvalues of the matrix $\underset{\sim}{E} + F\underset{\sim}{V}$ in the subspace of s- and p-states with $M_F = m$, $\underset{\sim}{\Delta}_{pp}^{(m)}$ is the diagonal submatrix of $\underset{\sim}{\Delta}_{pp}$ in the subspace of p-states with $M_F = m$ and Δ_{np} is the matrix element of $\underset{\sim}{\Delta}_{pp}$ labelled by the subscript n. Hence $\underset{\sim}{g}_{sp}$ can be written in the form

$$\underset{\sim}{g}_{sp} = -F \begin{pmatrix} \underset{\sim}{d}^{(0)} & 0 & 0 \\ 0 & \underset{\sim}{d}^{(-1)} & 0 \\ 0 & 0 & \underset{\sim}{d}^{(1)} \end{pmatrix} \underset{\sim}{V}_{sp} \underset{\sim}{\Delta}^{-1}_{pp} . \qquad (2.46)$$

II.4 Quench Radiation

If the radiation field is introduced as a first order perturbation (Hicks et al. 1972), the induced transition probability amplitude for the atom initially in state i at t=0 to be in the final state f together with a photon of frequency ω after a time τ is given, in the non-relativistic electric dipole approximation, as

$$c_f^{(1)}(\omega,\tau) = -\frac{i}{\hbar}\int_0^\tau dt_1 \int d\vec{r}_1 \; \psi_f^*(\vec{r}_1) e^{iE_f^* t_1/\hbar} e^{i\omega t_1} H'(\vec{r}_1)\psi(\vec{r}_1,t_1) \qquad (2.47)$$

where

$$H'(r) = -\frac{e}{m}\left(\frac{2\pi\hbar}{\omega V}\right)^{1/2} \hat{e}\cdot\vec{p} \quad . \qquad (2.48)$$

$\vec{p}$ is the momentum of the electron.

$\hat{e}$ is the polarization vector of the photon and v is the normalization volume for the photon. E_f is a real eigenvalue except for an infinitesimal negative imaginary part. For $\tau\to\infty$,

$$c_f^{(1)}(\omega,\infty) = -\sum_j (H')_{fj} \; g_{sj}(-E_f^*/\hbar-\omega) \qquad (2.49)$$

where the summation is taken over all intermediate states. The time dependence of the radiation integrated over all frequencies is obtained as (Drake and Grimley, 1975)

$$I(t) = 2\pi\hbar\,|d_f^{(1)}(t)|^2\,\rho(\overline{\omega}) \tag{2.50}$$

where

$$d_f^{(1)}(t) = -i\sum_j (H')_{fj}\, e^{iE_f^* t/\hbar} \sum_k e^{i\beta_k t}\,\mathrm{Res}\{g_{sj}(\omega_1)\}\big|_{\omega_1=\beta_k}\,, \qquad t>0\,. \tag{2.51}$$

The corresponding expression for the system of metastable hydrogen is deduced by Drake et al. (1975) Assuming that the initial state is an incoherent mixture of all four $2S_{1/2}$ hyperfine states with equal statistical weight, then (2.50) can be written in the form

$$I(t) = 2\pi\hbar\,\rho(\overline{\omega})\frac{|H'_{1s,2p}|^2}{4}\left(|\hat{e}\cdot\hat{F}|^2|A(t)|^2+|\hat{e}\times\hat{F}|^2|A'(t)|^2\right) \tag{2.52}$$

where

$$|A(t)|^2 = F^2 \sum_{\substack{F,M,F'\\ M=M'}} \Big|\sum_k e^{i\beta_k^{(M)}t}\,\mathrm{Res}\{B^{F,M}_{F',M'}(\omega_1)\}_{\omega_1=\beta_k^{(M)}}\Big|^2 \tag{2.53}$$

and

$$|A'(t)|^2 = F^2 \sum_{\substack{F,M,F'\\ M=M'\pm 1}} \Big|\sum_k e^{i\beta_k^{(M)}t}\,\mathrm{Res}\{B^{F,M}_{F',M'}(\omega_1)\}_{\omega_1=\beta_k^{(M)}}\Big|^2 \tag{2.54}$$

F, M and F', M' are the quantum numbers for the particular $2S_{1/2}$ and $1S_{1/2}$ states, respectively. $H'_{1s,2p}$ is the radial part of the matrix element

$$\Big\langle 1s \;\Big|\; -\frac{e}{m}\left(\frac{2\pi\hbar}{\omega V}\right)^{1/2}\hat{e}\cdot\vec{p} \;\Big|\; 2p\Big\rangle \;. \qquad (2.55)$$

$\rho(\bar{\omega})$ is the density of photon states $(\hbar\bar{\omega})^2 V/(2\pi\hbar c)^3$ per unit energy at the average frequency $\bar{\omega}=(E_{2s} - E_{1s})/\hbar$. The $B^{F,M}_{F',M'}$'s are given by

$$B^{0,0}_{F',M'} = \frac{\det(\underset{\sim}{\Delta}^{(0)}_{pp})}{\prod_{\ell}\hbar(-\beta^{(0)}_{\ell}+\omega_1)}\left(\Delta_{\nu}-3F^2\sum_{n'}\frac{\beta^{(0)}_{n'}}{\Delta_{n'p}}\right)\sum_{n}\frac{\alpha_n}{\Delta_{np}} \;, \qquad (2.56)$$

$$B^{1,0}_{F',M'} = \frac{\det(\underset{\sim}{\Delta}^{(0)}_{pp})}{\prod_{\ell}\hbar(-\beta^{(0)}_{\ell}+\omega_1)}\left(\Delta_{\mu}-3F^2\sum_{n'}\frac{\beta^{(1)}_{n'}}{\Delta_{n'p}}\right)\sum_{n}\frac{\alpha_n}{\Delta_{np}} \qquad (2.57)$$

and

$$B^{1,\pm1}_{F',M'} = \frac{\det(\underset{\sim}{\Delta}^{(\pm1)}_{pp})}{\prod_{\ell}\hbar(-\beta^{(\pm1)}_{\ell}+\omega_1)}\sum_{n}\frac{\alpha_n}{\Delta_{np}} \qquad (2.58)$$

where the hyperfine states $2P_{1/2}(F = 0)$, $2P_{1/2}(F = 1)$, $2P_{3/2}(F = 1)$ and $2P_{3/2}(F = 2)$ are labelled by 1, 2, 3 and 4, respectively. The coefficients α_n and $\beta_{n'}$ are summarized in Table I and II. $|A(t)|^2$ gives the intensity contribution for π-polarized radiation from $\Delta M_F = 0$ transitions whereas $|A'(t)|^2$ represents the intensity for σ-polarized radiation for which $\Delta M_F = \pm 1$.

If $\hat{F}$ is chosen to point in the x-direction and θ and ϕ are the spherical angles defining the direction of propagation,

TABLE I

Values of the coefficients α_n
in Eqs. (2.56), (2.57) and (2.58)

$n =$	1	2	3	4
$B^{0,0}_{0,0}$	0	1	2	0
$B^{0,0}_{1,\pm 1}$	0	∓ 1	± 1	0
$B^{1,0}_{1,0}$	1	0	0	2
$B^{1,0}_{1,\pm 1}$	1	0	0	-1
$B^{1,\pm 1}_{0,0}$	0	∓ 1	± 1	0
$B^{1,\pm 1}_{1,0}$	0	1	1/2	-3/2
$B^{1,\pm 1}_{1,\pm 1}$	0	1	1/2	3/2

TABLE II

Values of the coefficients $\beta_{n'}$
in Eqs. (2.56) and (2.57)

$n' =$	1	2	3	4
$\beta^{(0)}_{n'}$	0	1	2	0
$\beta^{(1)}_{n'}$	1	0	0	2

the total intensity observed experimentally can be obtained by summing over two mutually perpendicular vectors $\hat{e}$, both perpendicular to the direction of propagation. This is shown (Drake et al. 1975) to be

$$I(\theta,\phi,t) = 2\pi\hbar\rho(\bar{\omega})\frac{|H'_{1s,2p}|^2}{4}\{|A(t)|^2(\sin^2\theta + \cos^2\theta\cos^2\phi) + |A'(t)|^2(1 + \sin^2\theta\cos^2\phi)\} \qquad (2.59)$$

for the specific cases where the observation directions are parallel($\theta = \pi/2$, $\phi = 0$) and perpendicular($\theta = \pi/2$, $\phi = \pi/2$) to the electric field, the intensities are

$$I(\pi/2,0,t) = \pi\hbar\rho(\bar{\omega})\ |H'_{1s,2p}|^2\ |A'(t)|^2 \qquad (2.60)$$

and

$$I(\pi/2,\pi/2,t) = \pi\hbar\rho(\bar{\omega})\ |H'_{1s,2p}|^2\frac{|A'(t)|^2+|A(t)|^2}{2} \qquad (2.61)$$

respectively.

In the experiment a high speed beam of H(2s) particles travelling in the $\hat{z}$ direction with a velocity v enters an electric field at time t=0. The quench radiation along the beam is observed with a photon detector with a finite spatial resolution Δz along the beam axis. Fig. 2 shows the beat patterns $I_{/\!/} \equiv I(\pi/2,0,z/v)$ and $I_{\perp} \equiv I(\pi/2,\pi/2,z/v)$ for a typical beam velocity of 4.80×10^8cm/sec. Broading effects (see Appendix) due to a finite resolution $\Delta z \approx 0.19$mm have been

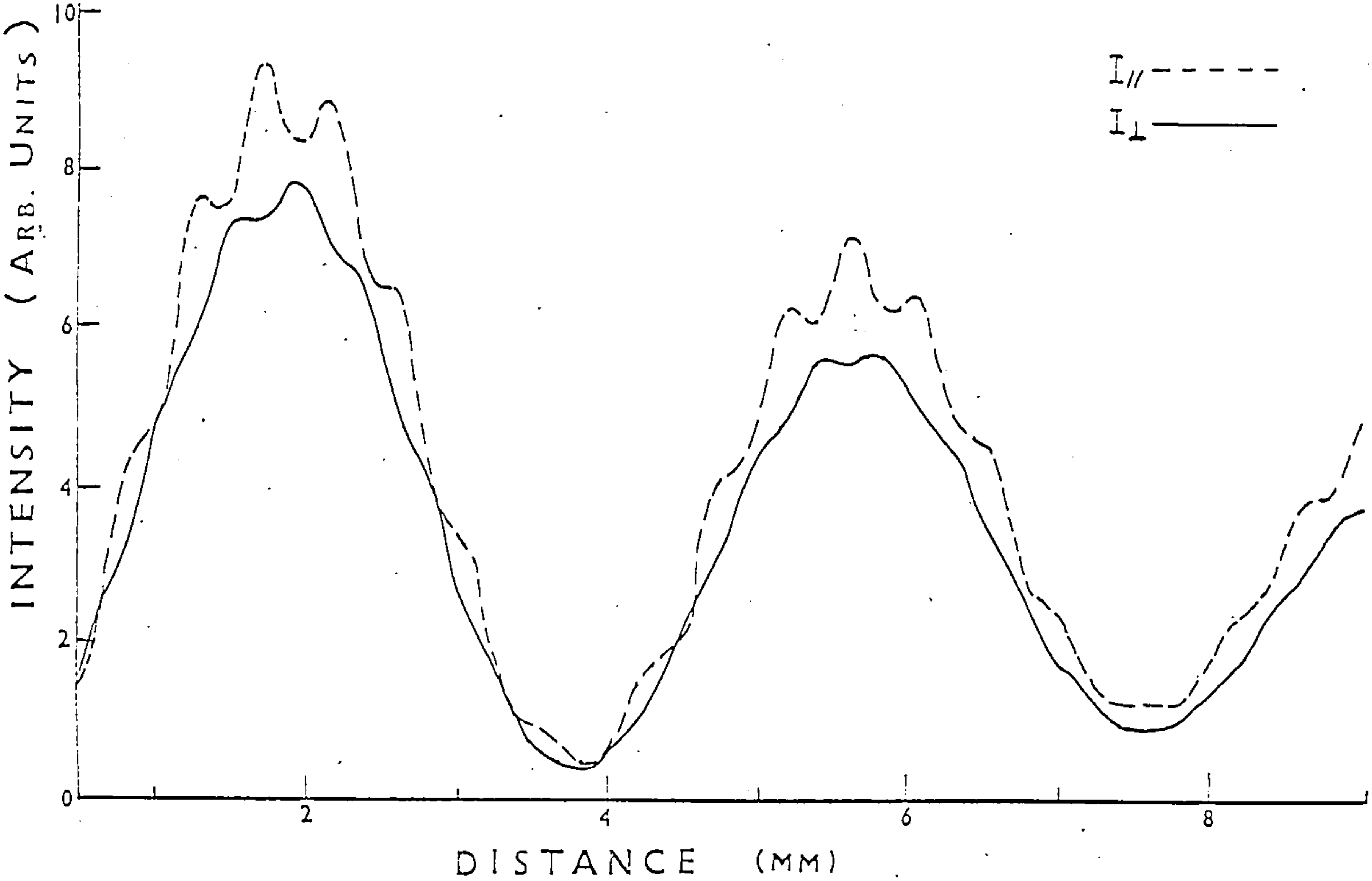

Fig. 2 Electric field-induced quantum beats in the intensities emitted parallel ($I_{//}$) and perpendicular ($I_{\perp}$) to the field direction.

folded into the theory. It is noted that the amplitude of the high frequency fine structure oscillation is much more pronounced in the radiation emitted parallel to the field direction than in the perpendicular direction. This is not surprising. The parallel intensity(Eq. 2.60) arises only from the $|A'(t)|^2$ term while the perpendicular intensity (Eq. 2.61) contains two terms, $|A'(t)|^2$ and $|A(t)|^2$, which are out of phase with each other.

In obtaining the theoretical curves it has been assumed that the beam entering the quenching field consists of an incoherent mixture of metastables in which all the hyperfine substates are equally populated. Thus the initial state amplitudes are precisely known. The assumption is made because the hyperfine interactions are weak and because in the experiment the metastables are not produced in a foil but by charge exchange in a gas cell at a long distance from the observation region.

CHAPTER III

EXPERIMENTAL

The apparatus for the production of a monoergetic beam of H(2s) particles is shown in Fig. 3. Here protons produced in a gaseous radio-frequency ion source I pass through an accelerating tube A, beam centering plates C and a magnetic field M for momentum analysis. The beam then traverses a differentially pumped gas cell, G.C. Leaving the cell are particles of all charge states. Since the electron capture cross-section into a state with principal quantum number n varies approximately as n^{-3} (Oppenheimer, 1928), the neutral beam also contains many excited states. With the exception of the $2S_{1/2}$ state, however, all other states have a short lifetime. Thus a metastable beam can always be obtained by waiting a sufficiently long time for all other states to decay to the ground state. To accomplish this the flight distance from the exit of the gas cell to the entrance of the observation region (Fig. 4) is kept large (65cm).

To reduce the noise in the observation region charged particles are deflected out of the beam by a small deflection field P.Q. (40V/cm), resulting in a beam of neutrals only, rich in metastable hydrogen. Since the quench radiation rate varies as the square of the field strength (see Section II.4), the small prequenching field does not destroy many of the metastable particles. Deflection of charged particles decreases the intensity of metastables in the observation region by not more than 10%.

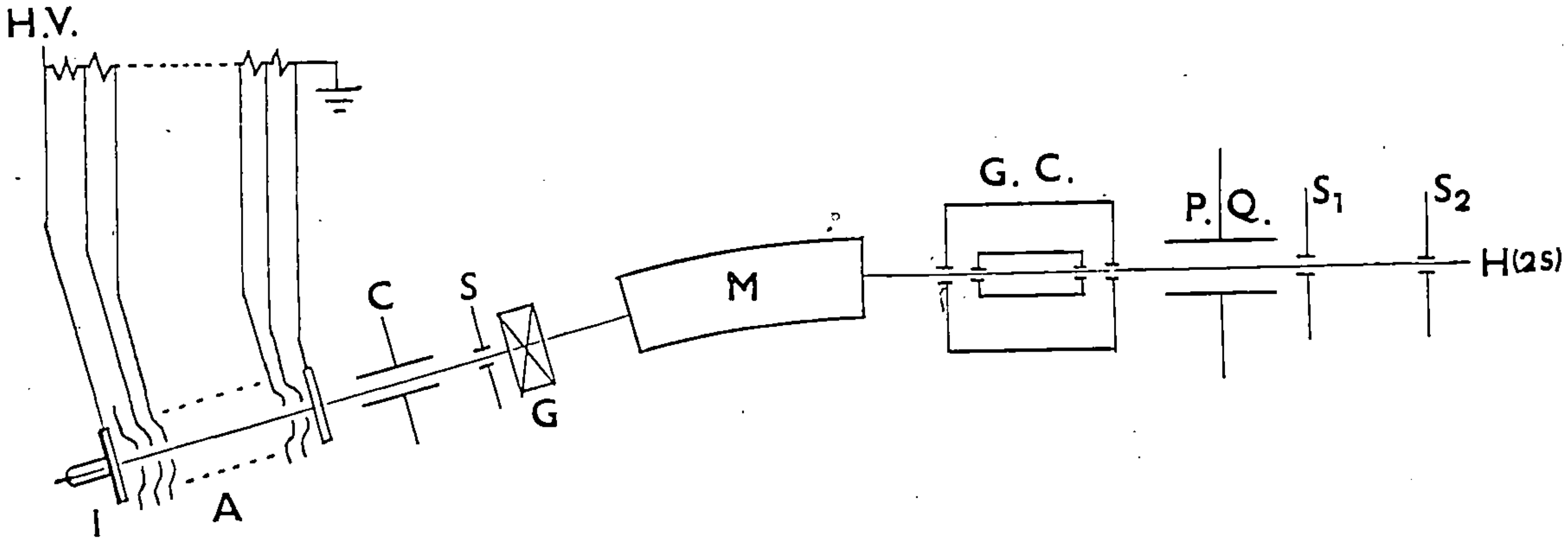

Fig. 3 Apparatus for the production of H(2s) beam.

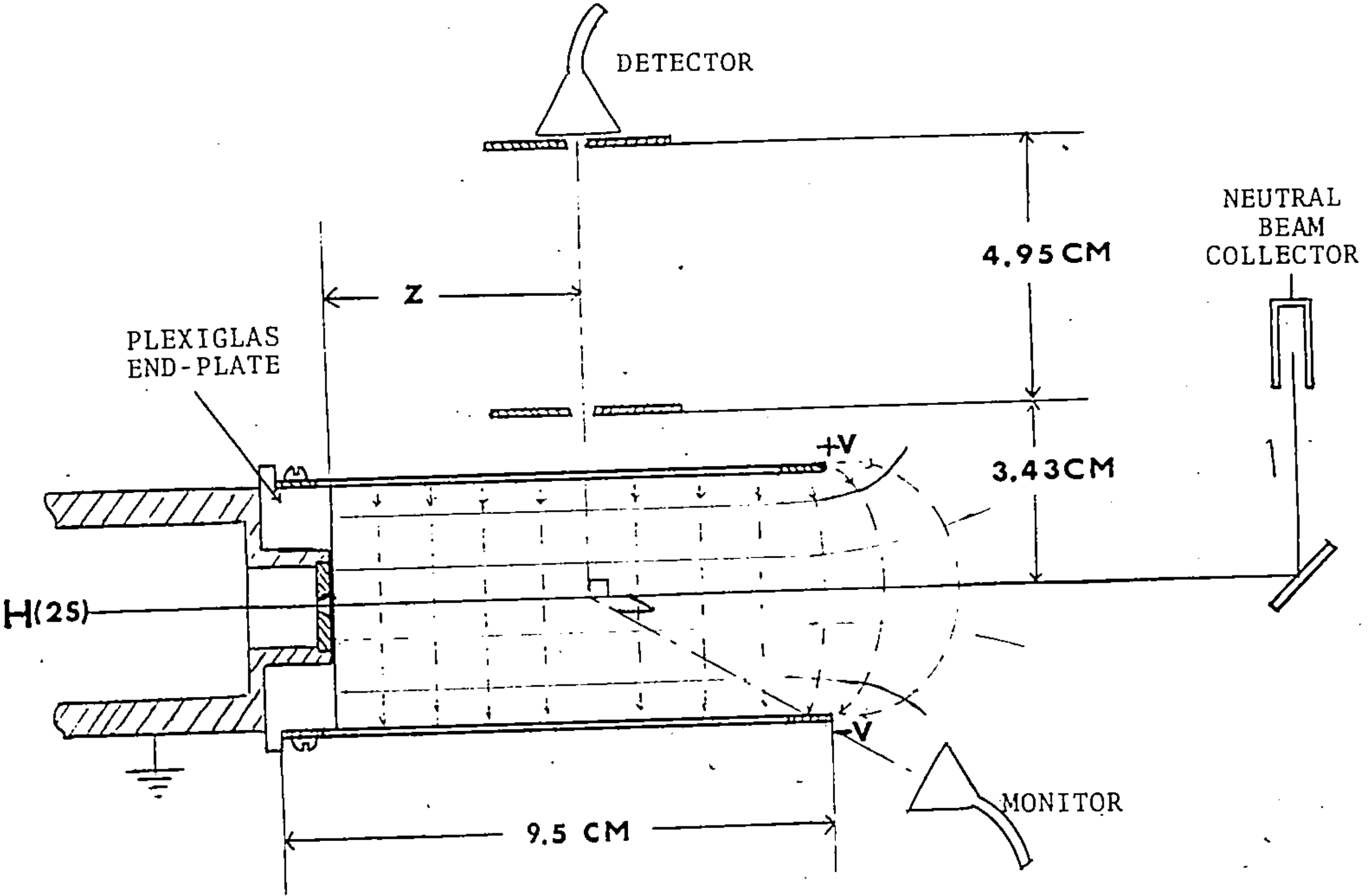

Fig. 4 Parallel plate quenching cell.

The slit system, S_1 and S_2 limits the angular divergence of the beam to 0.7 degrees. The beam entering the quenching cell (Fig. 4) has a circular cross-section of 1.3 mm^2.

The quenching cell consists essentially of a parallel plate capacitor mounted into a target chamber, which is pumped separately to a pressure of 4 x 10^{-7} torr. The quench radiation (Lyman -α photons, λ= 121.6 nm) is observed with a model BX762 Galileo Electro-Optics uv detector. The detection efficiency for Lyman -α photons is about 10% and the dark count is less than 0.5 sec^{-1}. The entire photon detection system, consisting of the uv detector and its slit system, can be translated with high spatial resolution along the beam axis. In this manner the intensity of the quench radiation can be observed as a function of distance. Since the beam velocity is constant, the observed Lyman-α emission pattern in effect represents the time evolution of the quenching process.

After traversing the quenching cell, the beam is made to impinge onto a brass surface from which the secondary electron yield is monitored. The output of the neutral beam detector is fed to a voltage - to - frequency converter to define an effective counting period, thus normalizing the signal to a pre-selected time-integrated particle flux.

In the energy range 4-120 keV, the secondary electron yield was found to be independent of the quenching field strength. This implies that the secondary electron yield is the same for the metastable particles as for the ground state atoms. This feature was exploited in the noise measurement (Section III.4).

III.1 Ion Source and Accelerating System.

The ion source (Fig. 5) consists of a pyrex ion bottle mounted on an aluminum base. Controlled amounts of hydrogen gas are leaked into the bottle by means of a palladium leak. An intense plasma is formed by exciting the gas by means of a 60 MHz radio-frequency field. A positive extraction potential drives the positive ions into the exit canal. A small axial magnetic field (~100 gauss) greatly enhances the probability for the plasma electrons to ionize neutral hydrogen atoms. Proton currents as large as 3mA emerge from the exit canal.

In some of our experiments, the required extraction potential was as large as 5kV. A disadvantage of such an extraction potential is that it introduces an energy spread amongst the ions leaving the exit canal. To see this, assume a uniform potential drop from the extraction electrode to the exit canal. Then an ion formed near the electrode undergoes an acceleration by the full extraction potential, whereas an ion originating near the quartz sleeve experiences negligible pre-acceleration. Thus a maximum energy spread $\Delta E \approx 5$keV would be predicted. However, we found experimentally that for an average beam energy of 120keV, $\Delta E \approx 1$keV. Therefore it appears that the vast majority of the ions originate from the region near the quartz sleeve.

The beam leaving the gap lens passes through an accelerating tube. A high voltage resistor rack supplied the appropriate potentials to the electrodes. The total voltage

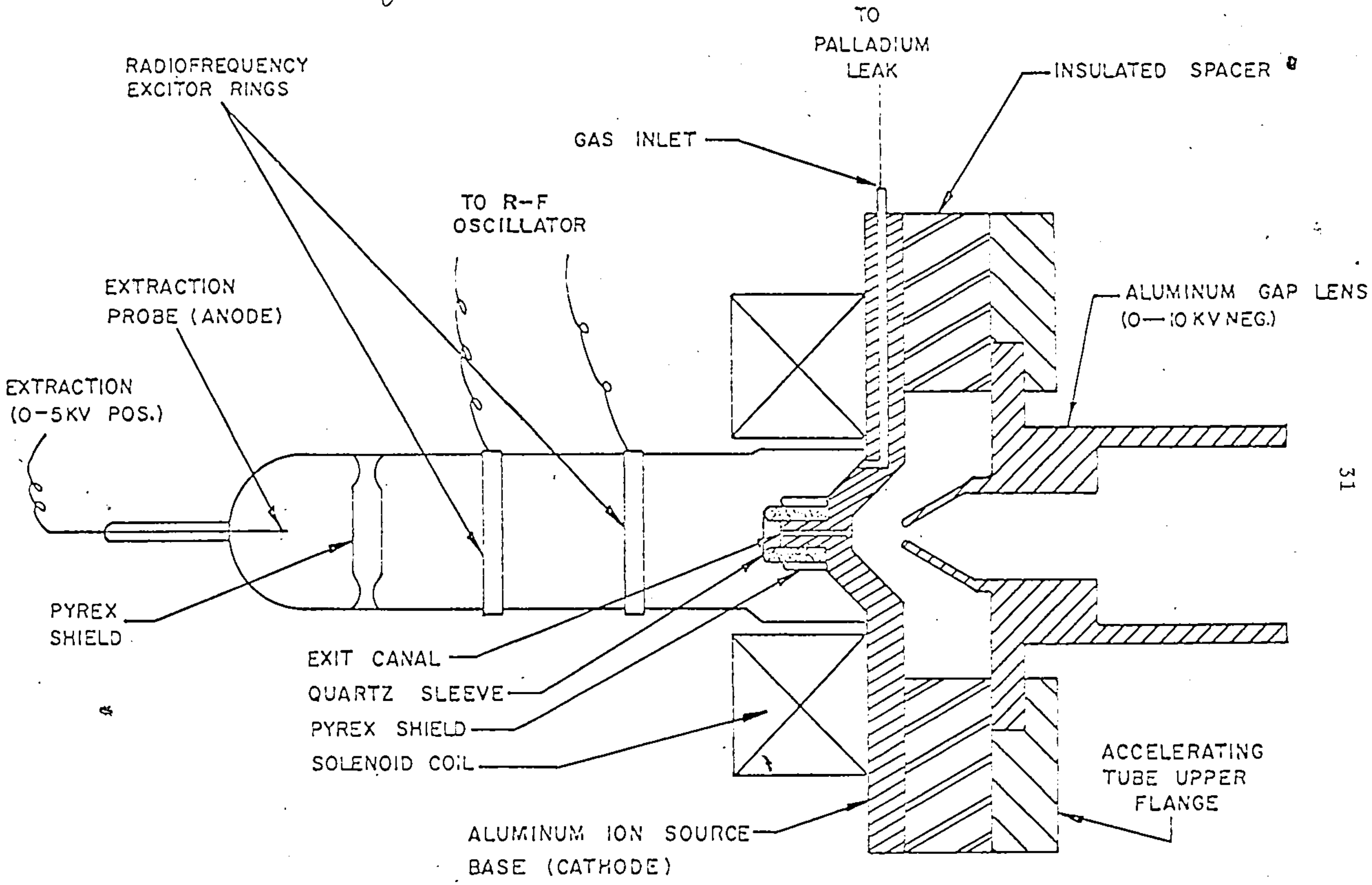

Fig. 5 Radio-frequency ion source.

across the accelerating tube is variable from 0 to 150 kV and is measured to an accuracy of ±2%. The beam leaving the accelerating column is steered through a 1mm wide slit into a 15° magnetic sector field by means of the centering plates C. A stability of at least one part in a thousand in the magnetic field was maintained by feeding the electromagnet with a John Fluke model 407D DC current supply. The magnetic analyzer reduces the relative energy spread $\Delta E/E$ of the beam to a value of less than 1/300. By using a gate valve G (Fig. 3), the ion source region and the magnetic analyzer section can be pumped separately. The ion source region is evacuated with a 6" mercury diffusion pump. A mercury pump instead of an oil pump is used to prevent the formation of insulating coatings on the accelerating electrodes. The magnetic sector is pumped with a 4" oil diffusion pump.

III.2 Gas Cell

The gas cell (Fig. 3) consists of a 15 cm long cylinder 3.8 cm in diameter with rectangular slits (0.10cm x 0.50cm) at each end. Gas is introduced through a variable leak. For the purpose of differential pumping, the cell is enclosed in a separate housing, which is pumped by a 6" diffusion pump. The housing contains slits of the same dimensions as those of the cell. Beside serving for collimation of the atomic beam, these slits provide the only openings between the housing and the other sections of the system. With the gas cell in operation the pressure outside the enclosure could be kept below 8×10^{-6} torr. When the variable leak to the gas cell was gradually opened the intensity of the neutral components in the beam first increased, reached a maximum and then decreased. By measuring the Lyman-α intensity in the quenching cell, we observed that the metastable particle current was proportional to the total current of the neutrals, which included ground state atoms. During an experiment, the leak rate was always adjusted for maximum metastable current. The value of this maximum was about five times as large with H_2 gas in the cell as with Ar. Since the cross-section for small angle multiple collisions between keV hydrogen ions and target atoms increases rapidly with the atomic number of the target atom (Lindhard et al. 1963) and since there is an extraordinary large cross-section for the destruction of metastables by Ar (Krotkov et al. 1972) this result is not surprising. Though the cross-section for formation of metastable hydrogen decreases (Dahlberg et al. 1968) as the beam energy increases from 10 keV to 130 keV, the H(2s) beam current was found to increase with increasing energy. Hence a sufficiently strong beam of metastable hydrogen could be obtained at an energy as high as 120keV. With a proton current of 10^{-7}A entering the gas cell an equivalent current of the order of 10^{-9}A of metastables was obtained. The metastable beam current was estimated from a measurement of the Lyman -α decay rate (Drake and Grimley, 1973), assuming a Lyman -α detection efficiency of 10%.

III.3 Quenching Cell

The quenching cell consists of a parallel plate capacitor (Fig. 4). The metal plates were mounted onto a plexiglas end-plate, the interior surface of which was coated with a thin but conductive layer of carbon such that the resistance between the plates was a few MΩ. The purpose of the coating was to greatly reduce the fringing field at the entrance hole. The electric field lines and the equipotential curves (solid lines) have been sketched in Fig. 4. With the potential applied as shown, it can be seen that the equipotential lines terminate perpendicular to the carbon coating. This is so because there is a <u>uniform</u> voltage drop across the uniformly coated carbon film. Except for a slight inhomogeneity of the field near the 1.5mm diameter entrance hole in the plexiglas plate, the field is uniform. Thus when a particle enters the hole, the electric field on it rises from zero to the full field value in a very short distance. Since the particles travel at great speed ($v \sim 2\text{-}4 \times 10^8$ cm/sec) the electric field is in effect switched on in a very short time

$$\Delta t = \Delta z / v \qquad , \quad (3.1)$$

where Δz is the effective fringing field distance. Since quantum beats can be observed only if the Hamiltonian changes in a time interval $\Delta t << f^{-1}$ where f is the beat frequency, we tried to keep Δz as small as possible.

Narrow slots (0.558cm wide) were cut into the rectangular (9.5cm x 8.89cm) capacitor plate for the observation of the quench radiation.

III.3.1 End Plate

Since slight irregularities in the carbon film can distort the field, great care was taken in the machining of the rectangularly shaped (4.57cm x 8.89cm) plexiglas end-plate (Fig. 6) and in the preparation of the carbon coating. The end-plate was constructed out of commercially available plexiglas which has a protective layer of paper over its surface. To prevent scratches or dirt particles on the surface from being coated, the paper from it was removed at the very last step in the machining process. The end-plate was then washed in clean methanol. To minimize the fringing field distance it was found that the thickness t near the entrance hole had to be made as small as possible. A t-value below 0.75mm would distort the shape of the carbon coated surface.

It was also necessary to coat the entrance side with a conducting layer (Al) to ensure that the beam travels at ground potential just before it enters the quenching cell. For this reason the metal entrance slit, defining the beam diameter(1.3mm), makes electrical contact with the Al-layer.

Two narrow strips of silver (0.5mm wide) were vacuum-deposited on the two longer edges of the inner surface. Brass binding posts were glued into holes at the corners of the plexiglas end-plate to make contact with the low resistance silver strips. Electrical contact between the posts and the silver strips was made with silver paint. Next carbon was vacuum-deposited over the entire surface, including the silver

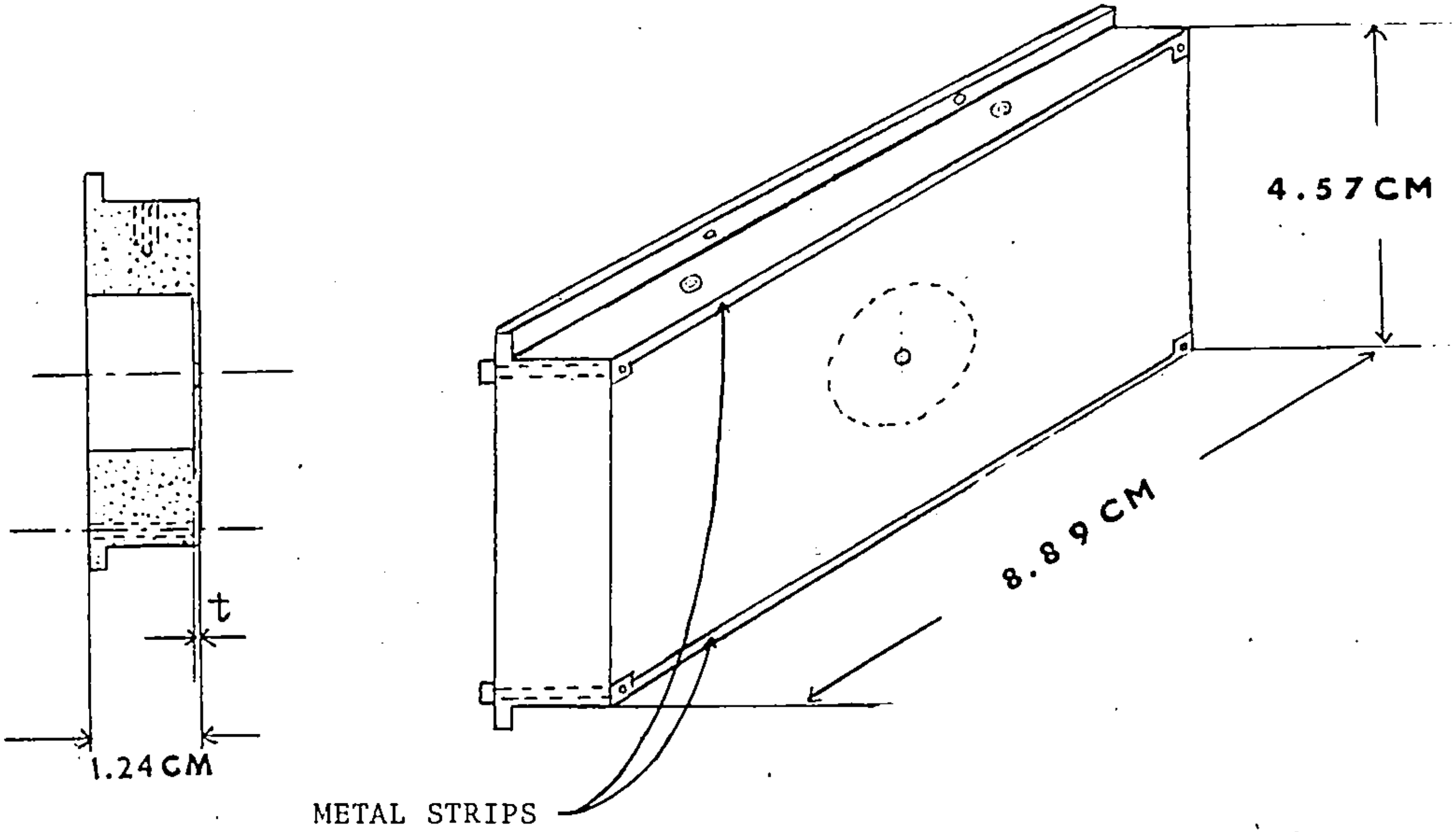

Fig. 6 Carbon coated plexiglas end-plate for the quenching cell in Fig. 4.

strips. The capacitor plates were then mounted to the plexiglas end-plate and electrical contact was made with the binding posts at the back surface.

Carbon deposition was accomplished by mounting the plexiglas end-plate above a carbon arc in vacuum. Although the thicker carbon layers were generally found to be more uniform, only thinner layers with a high resistance (above 2MΩ) could be used. Joule-heating destroyed the thicker films when the quenching field was applied.

The field on the beam axis is nearly given by that of a parallel plate capacitor, $F=2V/d$ (Fig. 4). Deviations from this value arise because of the presence of the narrow slots in the capacitor plates and the grounded slits of the photon detection system. More accurate values of the quenching field were obtained by solving La Place's equation numerically, subject to the boundary conditions. The field thus calculated was accurate only to about ±1% owing to irregularities in spacing between the thin capacitor plates.

III.4 Photon - detection

III.4.1 Translation of Detector

Fig. 7 shows how the detection system could be translated with high spatial resolution along the beam axis. The detector and its slits were rigidly mounted onto a base plate. The plate was moved by means of a fine threaded precision screw (20 threads/cm) against the force of strong springs. Spring loading avoids the normal problems of backlash. The screw was rotated by means of an adjustable

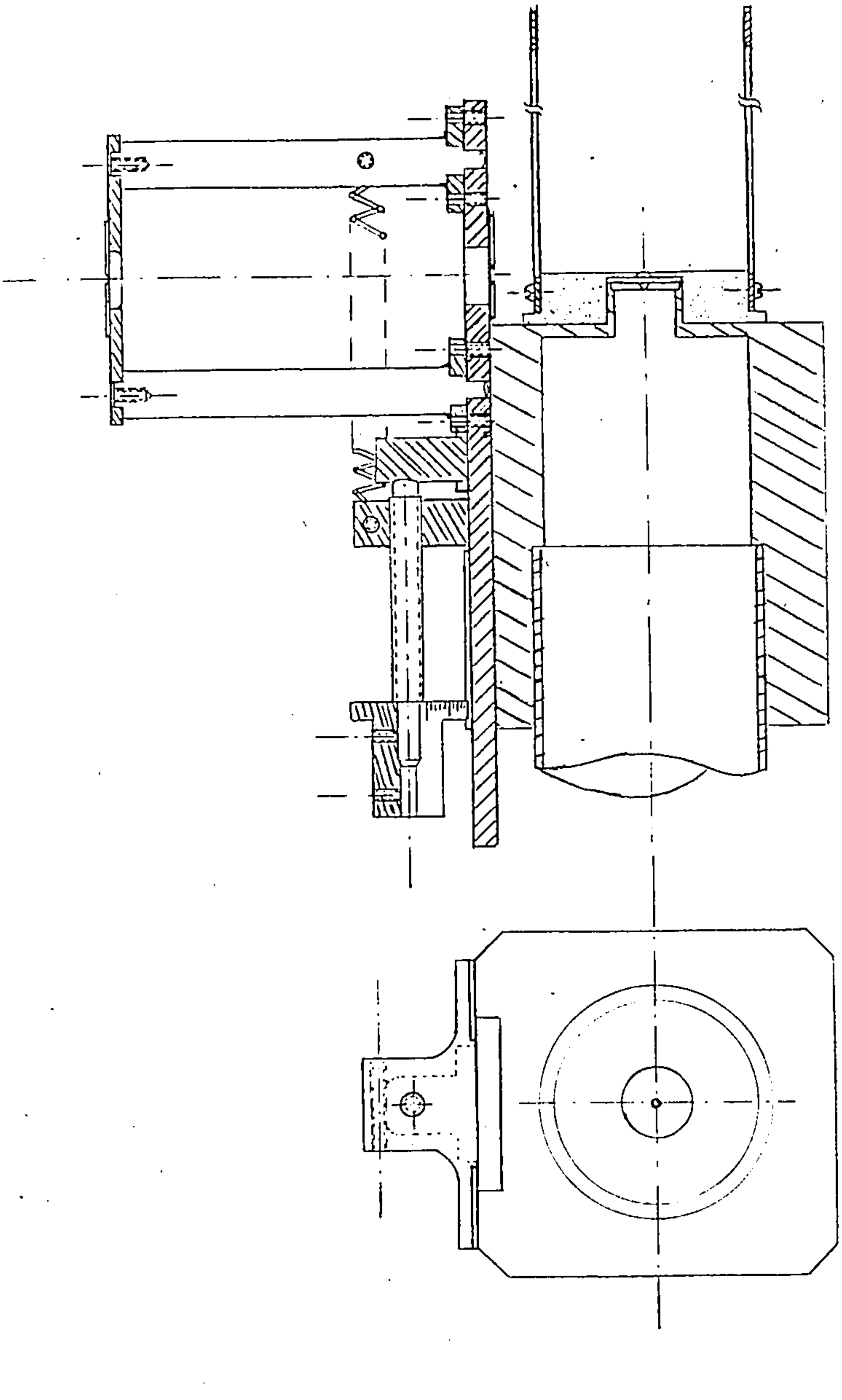

Fig. 7 Translation mechanism for the detector system.

metal cable and the position of the detector was read from a dial to a relative accuracy of ±5x10^{-3}cm. The absolute value of the position z (Fig. 4) (the distance between the viewing axis defined by the slit system and the carbon coated plexiglas surface) was measured with an accuracy of ±0.2mm. The difficulties in determining this value with precision arose from reflections of light from the carbon coated surface and from deviations in its flatness. This surface could not be machined (See Section III.3.1). Because of spatial limitations, the translational movement of the detector was limited to 2.5cm.

III.4.2 Slits

The slit distances from the beam axis were 3.43cm and 8.38cm for the inner and outer slits respectively. For these fixed distances, the widths were chosen for optimum spatial resolution. To fulfill this condition for Lyman-α photon detection, the slits could not be made narrower than 0.1mm and had to be of unequal width otherwise the resolution would have been seriously limited by Fresnel diffraction. This is discussed in the Appendix. The dimensions of the rectangularly shaped inner and outer slits were 0.20mm x 15mm and 0.15mm x 15mm respectively.

III.4.3 Electronics and Monitoring System

A block diagram of the electronics is shown in Fig.8.

The output pulses from the uv counter passed through a preamplifier (Ortec 113) to an amplifier (Ortec 485) which in turn fed a single channel analyzer (Ortec 406A) to produce the

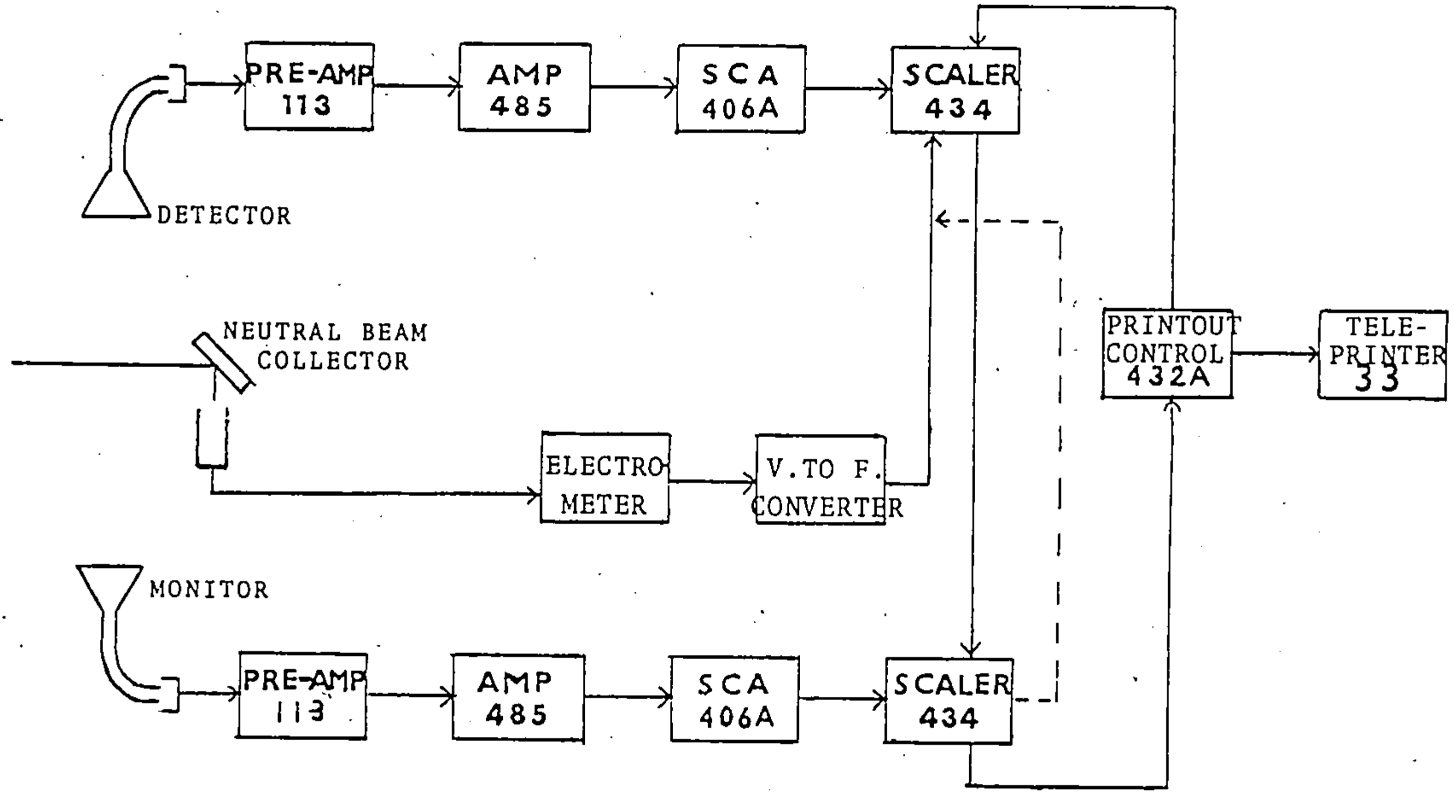

Fig. 8 Block diagram of electronics.

logic signal for the scaler (Ortec 434). The digital output was recorded on paper tape with a teleprinter (Teletype model 33), controlled by a printout control (Ortec 432A). The scaler of the counting system was gated from the monitoring system.

An accurate observation of the intensity pattern of the quench radiation required that photon counts at different positions of the detector could be determined for precisely equal numbers of metastables. Since the beam intensity (and probably also its metastable content) varied in time by as much as ±2% a monitor system was employed to produce an external timing reference for the scaler of the detection system. For this purpose another uv detector was used which viewed the quench radiation perpendicular to the field direction over a large solid angle (Fig. 4). The viewing region extended over a region of 6cm of the beam axis, including the region near the plexiglas end-plate, thus ensuring that the counting rate of the monitor was at all times proportional to the intensity of the metastables. To obtain the large viewing distance on the beam axis, the counter was positioned at an angle of about 60° to the beam path. The output logic pulses from the electronics of the monitor counter were also fed into a 434 Ortec scaler. The scaler was modified to obtain an output pulse for five different values of accumulated counts, each differing by a factor of ten. The output pulse was employed to trigger the time switching network of the scaler in the detection system, thus normalizing the signal counts to a preset number of monitor counts. Since the quenching rate was field dependent, the normalization was too.

Since the monitor kept track of the metastables rather than neutrals, errors arising from possible variation in the efficiency for electron capture into the 2S states in the gas cell and from beam current fluctuations were eliminated. A disadvantage of the uv monitor is that it is field dependent. Since we were interested in the radiation pattern only at constant field strengths, this disadvantage did not result in any serious limitation.

The neutral beam detector could also be used as a monitoring device. A time-integrated particle flux of neutrals was registered for pre-selected number of counts from the voltage - to - frequency converter. A disadvantage, however, was that the secondary electron yield from its brass surface was slightly time dependent. The coefficient of secondary electron emission changed under prolonged ion bombardment by as much as ±10%. The neutral beam detector had to be used for the determination of noise.

III.5 Noise

The signal observed in the presence of a quenching field must be corrected for noise counts. We defined the background noise as the counts still obtained with the quenching field turned off. The correction requires that the noise and the signal be determined for an identical beam flux. A measure of the beam flux which was independent of the quenching field was obtained by integrating the neutral beam detector output over the time interval of each measurement. This served to normalize the noise and signal measurements to the same beam flux, even though these quantities were determined at different field strengths. Since the efficiency for the secondary electron emission of the neutral detector changed slowly with time (see Section III.4.3), the resulting uncertainty in the noise measurement was as large as 5%

The measured noise is of the form

$$A+Be^{-\gamma z/v} \tag{3.2}$$

where z is the position of the photon detector relative to the entrance hole of the quenching cell and $\gamma=6.2\text{x}10^{8}\text{sec}^{-1}$. The first term represents a constant background noise which presumably arises from the occasional collision between a fast ground state atom and the residual gas. The second term originates from the decay of 2P states, which decay at the rate γ. Because of their short lifetime, almost none of the atoms leaving the gas cell in the 2P states survive the long distance (65cm) to the observation region. It appeared that the 2P components of the noise were created along the beam by collisions between metastables and thermal gas atoms before the beam entered the quenching cell. In the range of beam energies (46-120keV) investigated, the dominant contribution to the noise arose from the second term in expression (3.2). Since B decreased rapidly with increasing energy while A increased slowly, the noise count was much lower at high beam energies. Although the energy dependence of B is not understood, it is likely that its behavior is correlated with multiple small-angle collisions, the probability of which decreases rapidly with increasing energy (Lindhard et al. 1963). Thus it seems that at lower energies some of the small angle collisions amongst the particles in the beam itself result in the production of atoms in the 2P states.

The noise measurements for the 46keV and 120keV beams are shown in Figs. 9 and 10, respectively, where the solid curves are given by (3.2). For the 46keV beam the values of A and B are 0.00170±0.00058 and 0.0408±0.0013 respectively. For the 120keV beam the corresponding values are A=0.00506±0.00087 and B=0.0034±0.00054.

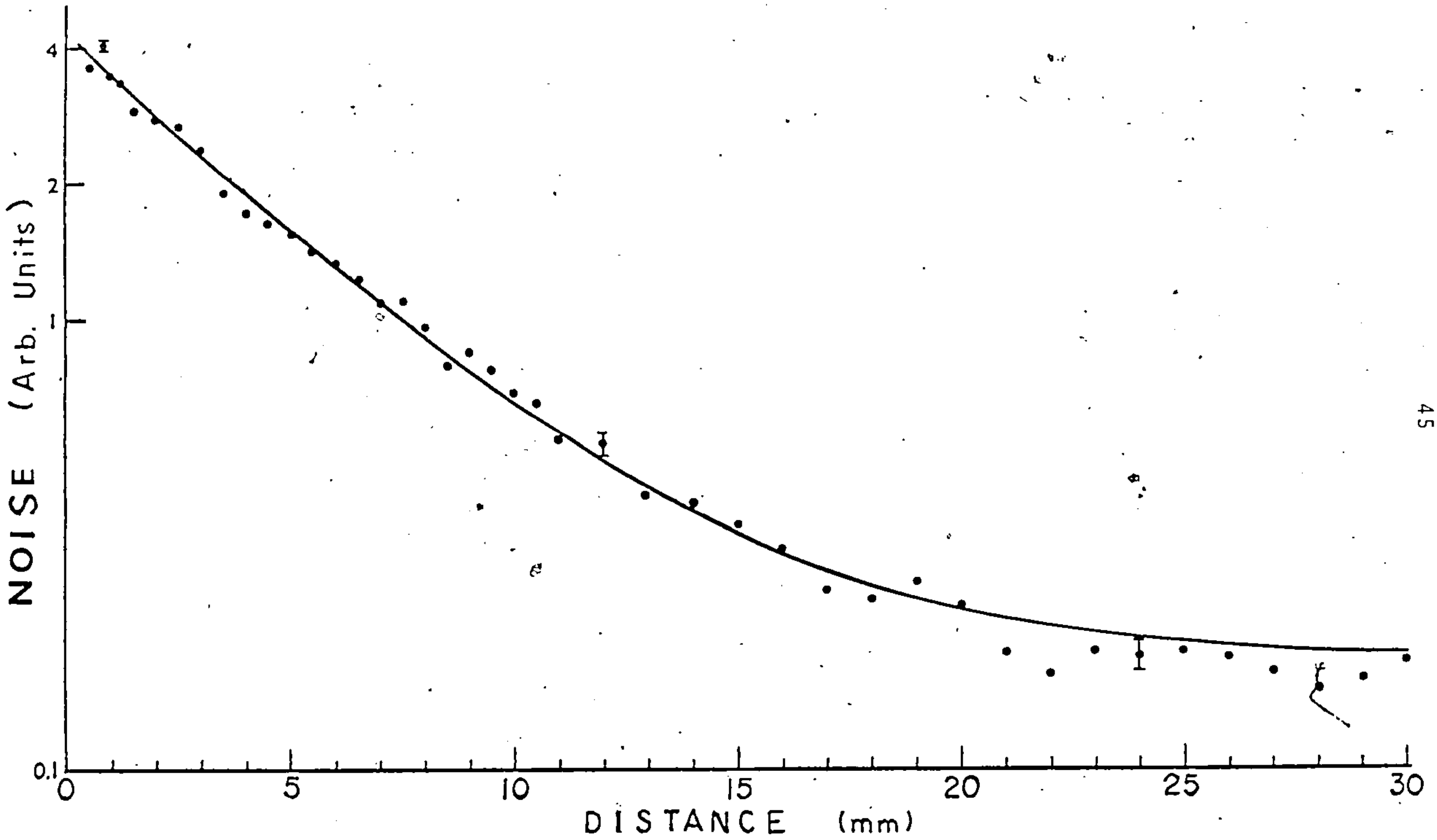

Fig. 9 The distance dependence of the noise at a beam velocity of 2.97 x 10^8 cm/sec. The solid curve represent (3.2).

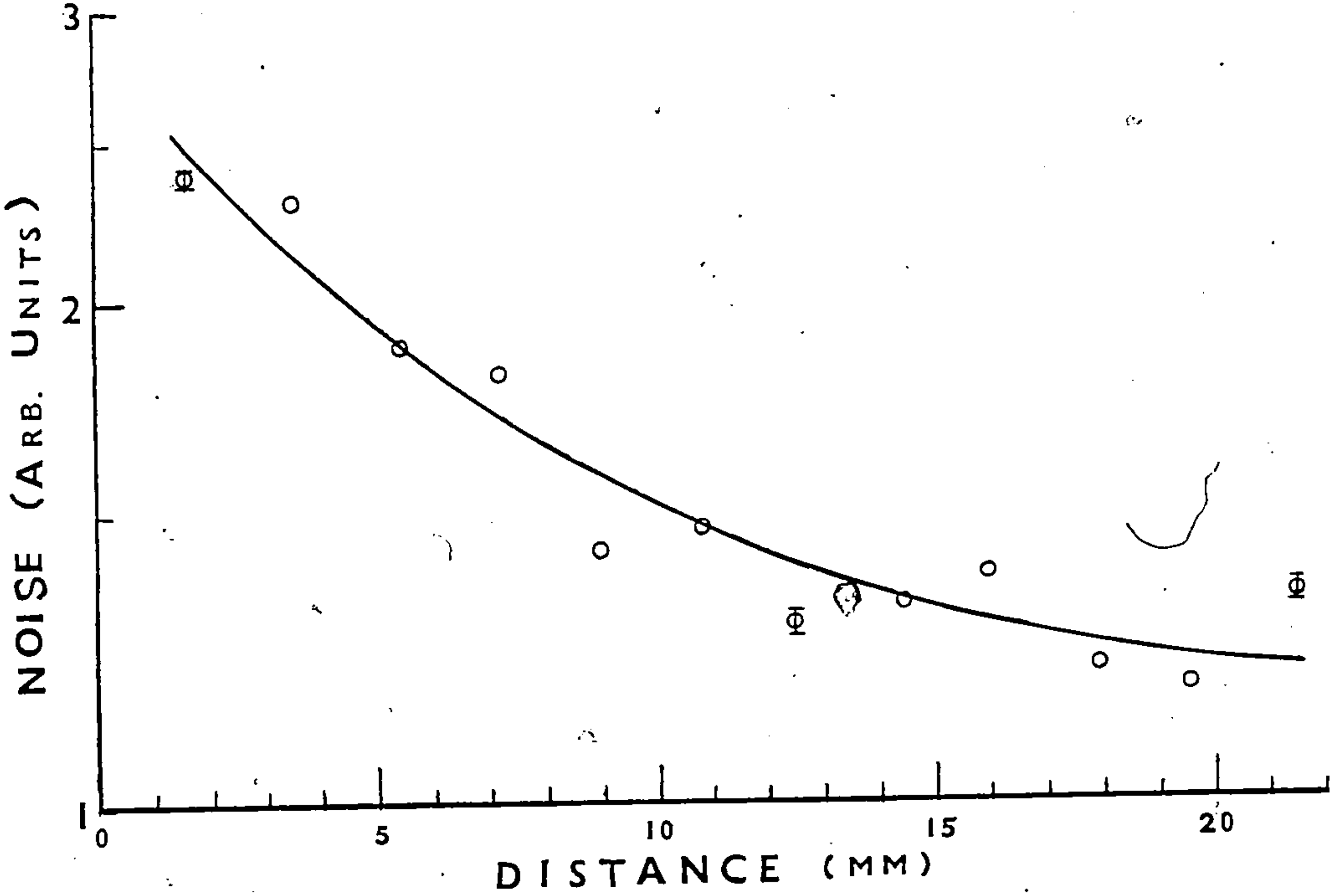

Fig. 10 The distance dependence of the noise at a beam velocity of 4.80 x 10^8 cm/sec. The solid curve represent (3.2).

CHAPTER IV

RESULTS

Since the photon detection system could only be translated over a distance of 2.5cm, experiments were carried out at two beam velocities, $v=2.97\times10^8$cm/sec (46keV) and $v=4.98\times10^8$cm/sec (120keV). At the lower velocity a relatively long time interval for observation falls within the range of the detector, whereas at higher velocity, the intensity pattern on the beam axis is spread out over a greater distance, whereby the time resolution is increased.

IV.1 Quantum Beats at Lower Velocity

The 46keV data have been summarized in Figs. 11, 12, and 13 for various values of quenching fields. Each experimental point, corrected for noise, contains at least 2000 counts obtained in an average time interval of 100 sec. The maximum statistical error is roughly the size of the points. The dashed curves are theoretical and assume that the field is switched on infinitely fast. The slit function, which includes an allowance for Fresnel diffraction effects, is folded into the theoretical calculation. In all three figures, the only adjustable parameters are an overall vertical scaling factor and a small horizontal shift $\Delta z \approx 0.10$mm. Although this shift may be related to the finite switch-on-time of the quenching field, its value is consistent with the uncertainty in the absolute location of the beam entrance hole along the beam axis. The main oscillations at about 10^3 MHz correspond

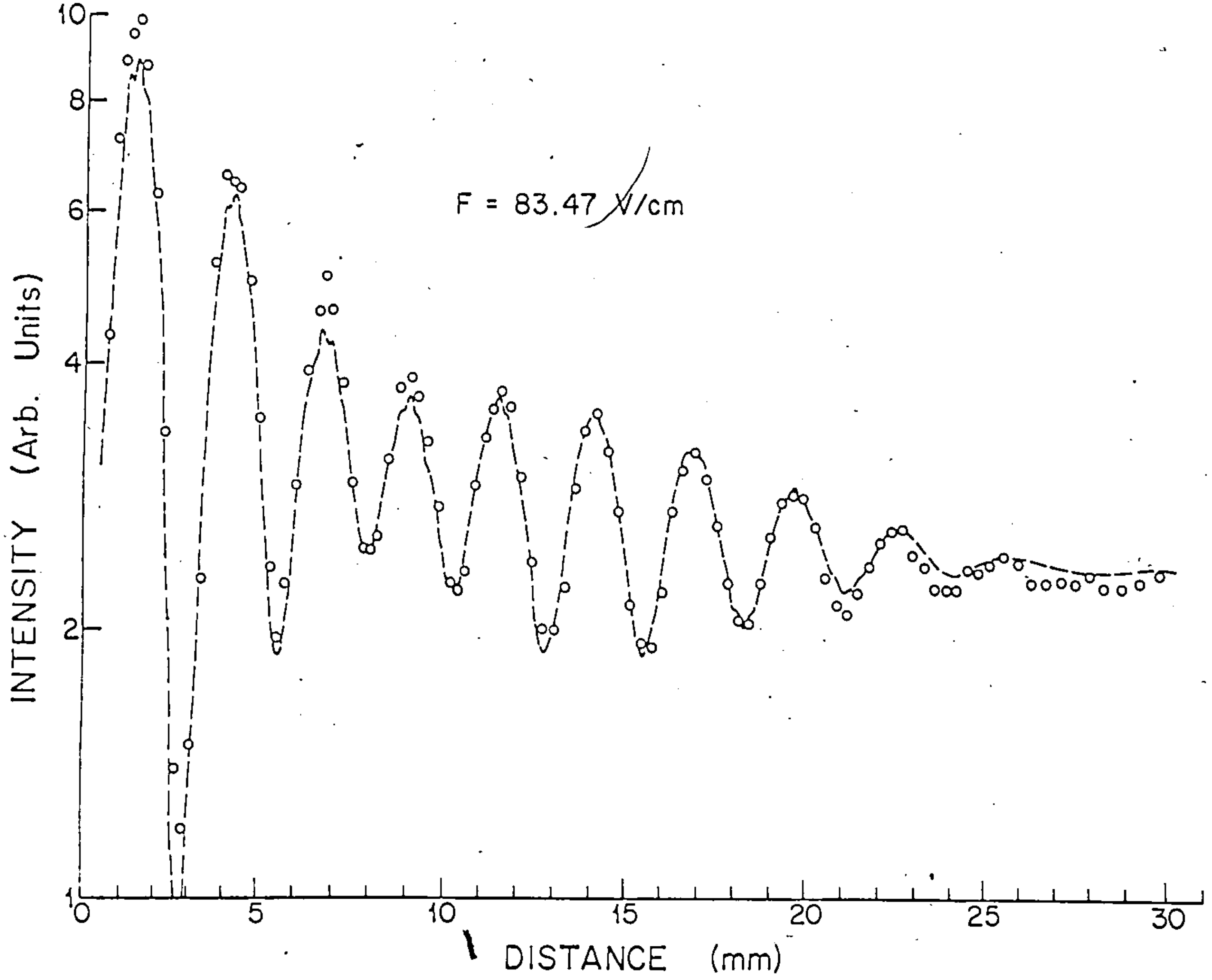

Fig. 11 Comparison of the theoretical (dashed curve) and experimental (circles) beat pattern for a beam velocity of 2.97×10^8cm/sec and a quenching field of 83.5 V/cm.

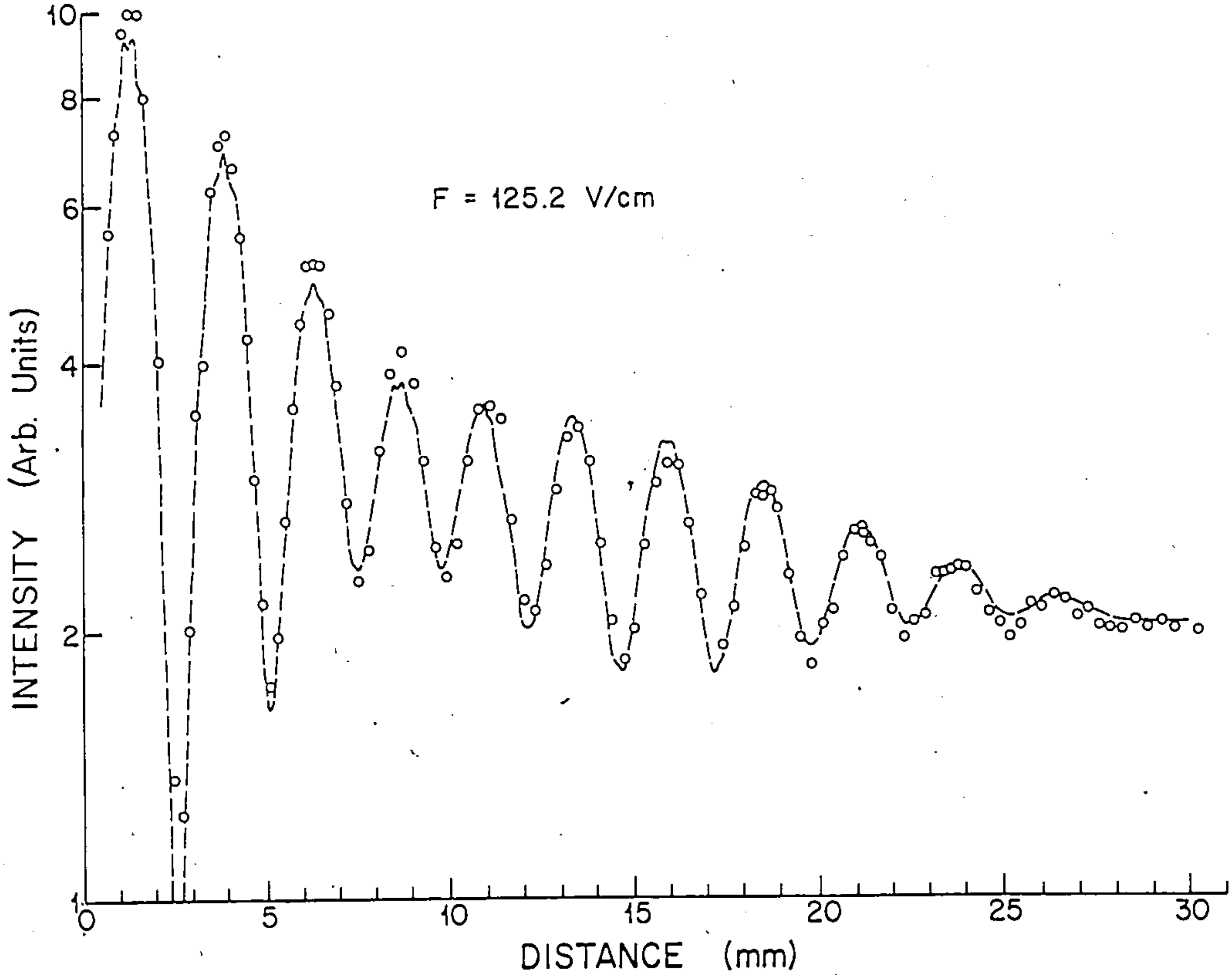

Fig. 12 Comparison of the theoretical (dashed curve) and experimental (circles) beat pattern for a beam velocity of 2.97×10^{8}cm/sec and a quenching field of 125 V/cm.

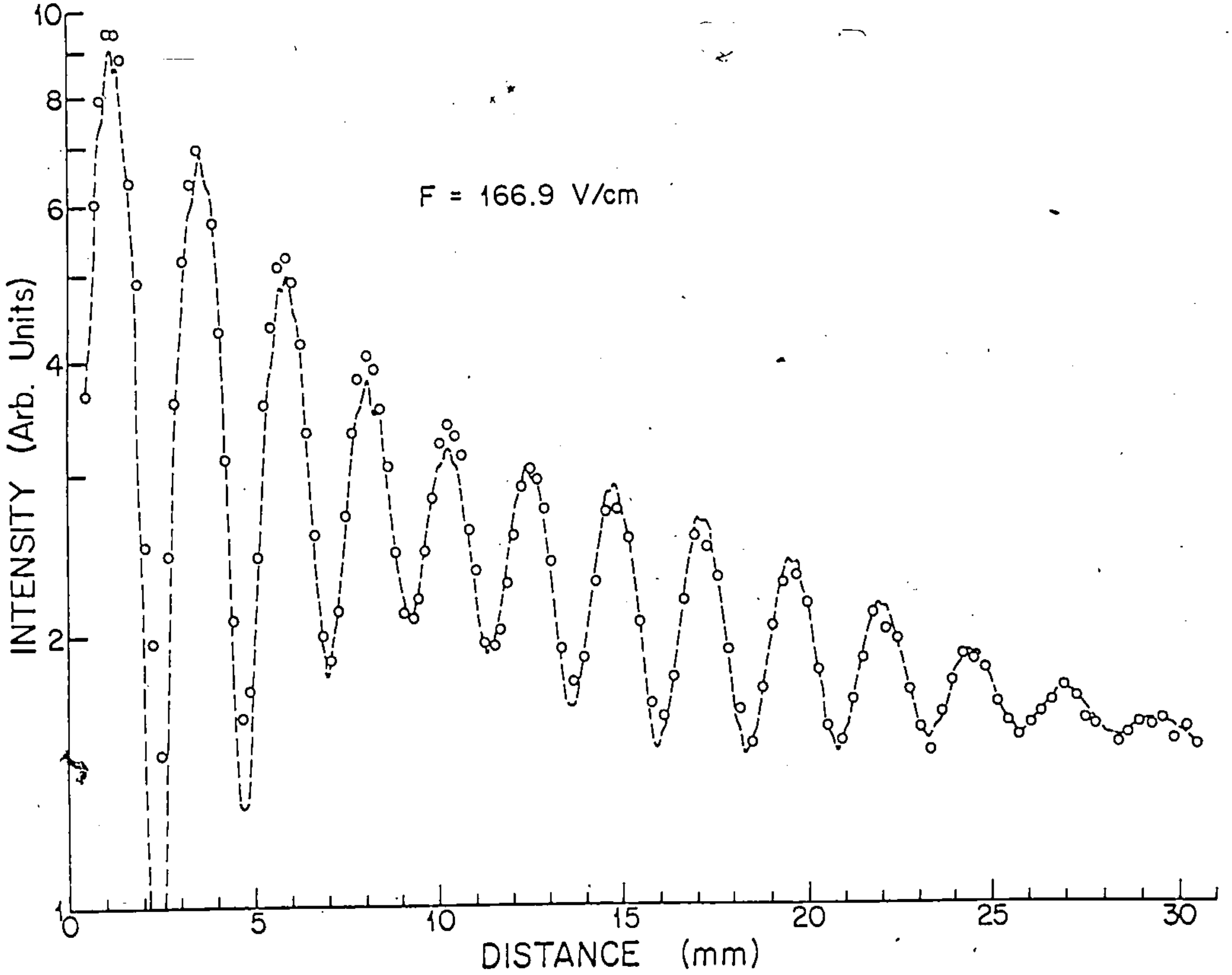

Fig. 13 Comparison of the theoretical (dashed curve) and experimental (circles) beat pattern for a beam velocity of 2.97×10^8cm/sec and a quenching field of 167 V/cm.

to the beats at the Stark-shifted Lamb-shift ($2S_{1/2}$-$2P_{1/2}$) frequencies. The modulation superimposed on the curves has a frequency of about 180 MHz and arises from interference between the hyperfine structure of the $2S_{1/2}$ and $2P_{1/2}$ states. The zero-field hyperfine structure splitting of the $2S_{1/2}$ state is 177MHz.

When the field is decreased by a factor of two from 167 V/cm to 83.5 V/cm, the main beat frequency decreases by a factor of 1.15. Apparently the agreement between theory and experiment deteriorates somewhat with decreasing field strength. This can probably be accounted for by uncertainties in the measurements. Since the quenching rate is proportional to the square of the field, the <u>average</u> signal-to-noise ratio decreases at lower field. At 167V/cm the noise corrections at the first observed maximum and minimum are 7% and 29%, respectively, and the corresponding corrections at 83.5V/cm are 2% and 59%. Although the relative magnitude of the noise decreases with distance (Eq. 3.2) it remains large, particularly for the minima, at low quenching fields and errors become important. Because of this and because of the perturbing effects of stray fields, a comparison between theory and experiment is most reliable at higher quenching fields, where the overall agreement is good. It appears that at lower quenching fields there are discrepancies between theory and experiment for the overall decay rate. However, it was found, using a Fourier analysis, that the various frequencies in the beat pattern are very insensitive to this decay and large errors in it do not significantly affect the final numerical results.

IV.2 Quantum Beats at Higher Velocity

It may have been noticed that the predicted (Section II.4) rapid $2S_{1/2}$-$2P_{3/2}$ fine structure oscillation at about 10^4MHz was not resolved in Figs. 11, 12 and 13. To improve the time resolution the beam energy was increased from 46keV to 120keV. The results for a quenching field of 167V/cm and for two new plexiglas end-plates are shown in Fig. 14, where solid lines have been drawn through the experimental points. The fine structure oscillations have been clearly resolved. To obtain the best overall agreement with theory (dashed curves) the experimental points were shifted by 0.4mm, in a direction downstream of the entrance hole. The statistical errors on the points are similar to those at 46keV, but the noise counts at 120keV are about a factor of three lower (Section III.5). At the first observed maximum and minumum the noise corrections are 2% and 15% respectively.

IV.3 Phase Shift

The most significant difference between theory and experiment is the phase shift of the rapid oscillations. Even though the data in Fig. 14 were obtained with entirely different end-plates, the apparent phase shift is the same. Thus it appears that spatial variation of the electric field along the beam axis near the entrance hole has little effect. The data for Fig. 14(a) were obtained with a plexiglas end-plate where the periphery of the carbon coated entrance hole

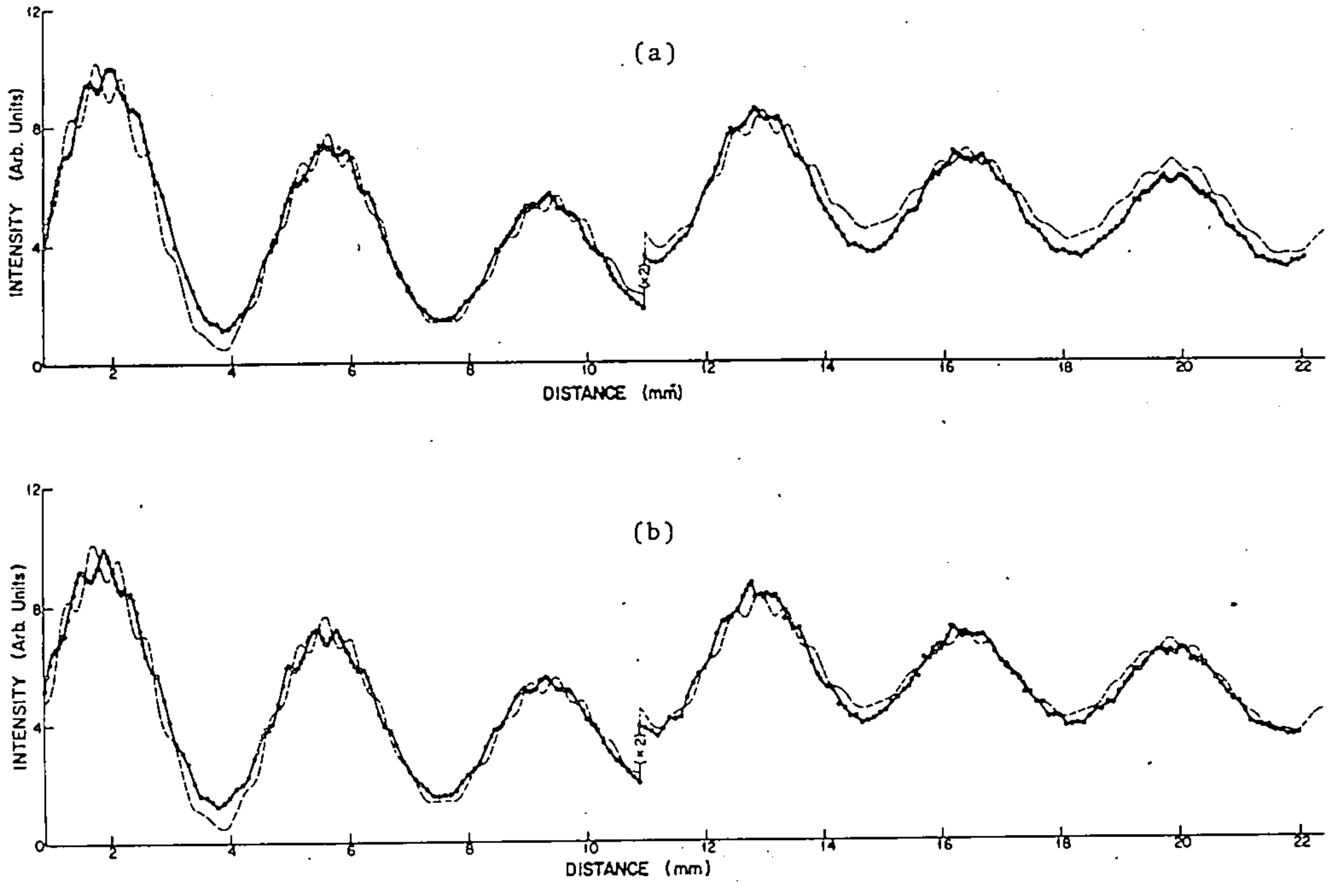

Fig. 14 Comparison of theoretical (dashed curves) and experimental (solid curves) beat pattern for a beam velocity of 4.80 x 10^8 cm/sec and a quenching field of 167 V/cm. Fig. 14(a) and Fig. 14(b) were obtained with different plexiglas end-plates for the quenching cell.

made electrical contact with the aluminum coated surface at the back. Since contact ensures that the periphery of the entrance hole is grounded, there cannot be any overshoot of the electric field in the hole region. Thus when a particle enters the quenching cell the electric field on it will gradually rise from zero to its full field value. The data for Fig.14(b) were obtained for an end-plate in which electrical contact between the carbon coated periphery and the aluminum coating at the back had purposely been destroyed with the aid of sandpaper. In this case the electric field at the entrance hole is expected to be larger than the field inside the quenching cell. Nevertheless we were able to show that the phase shift can be affected by the end-plate. A new run with yet another end-plate yielded results (Fig. 15) of much poorer quality in resolution but with no apparent phase shift. Because the various phase shift data seem to be contradictory no conclusions have been drawn. Since for our particular geometry, we have not been able to calculate the field on the beam axis near the entrance hole, no further experiments on the phase shift have been carried out.

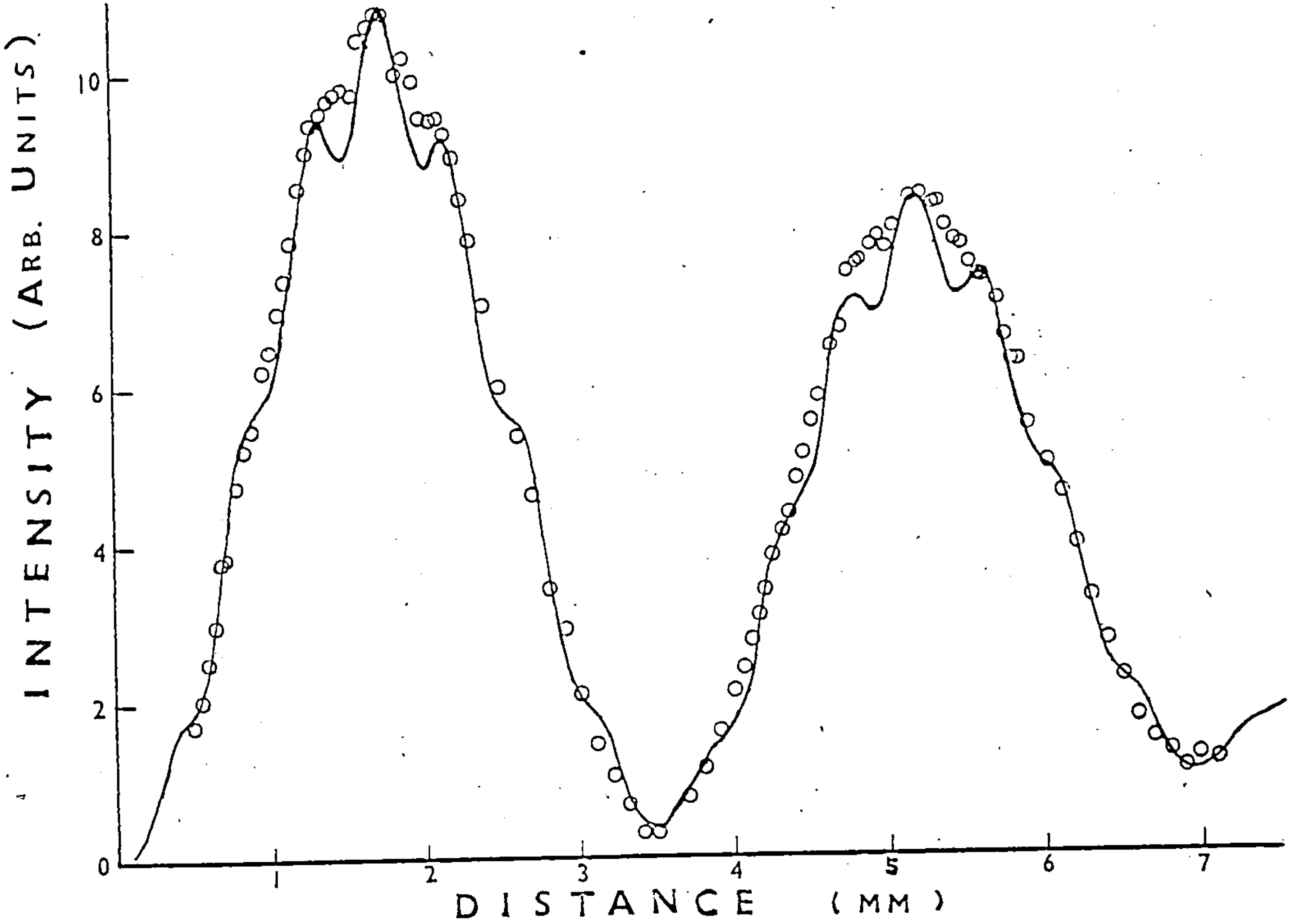

Fig. 15 Comparison of theoretical (solid curve) and experimental (circles) beat pattern for a beam velocity of 4.80×10^8 cm/sec and a quenching field of 209 V/cm.

CHAPTER V

ANALYSIS AND CONCLUSION

V.1 Analysis of Experimental Data

To find the various frequencies in the observed quantum beat patterns, a Fourier analysis was performed. Let L be the maximum translation of the detection system. It is convenient to divide L into an even number, 2n, of equal distance intervals d. The signal intensity I(z), which is proportional to the radiative emission rate, can then be expressed as

$$I(z) = I(sd) = \sum_{k=0}^{n} a_k \cos\frac{2\pi ksd}{L} + \sum_{k=1}^{n-1} b_k \sin\frac{2\pi ksd}{L}, \qquad 0 \leqslant s \leqslant 2n \tag{5.1}$$

with

$$a_0 = \frac{1}{2n} \sum_{s=0}^{2n-1} I(sd) \tag{5.2}$$

$$a_{k'} = \frac{1}{n} \sum_{s=0}^{2n-1} I(sd) \cos\frac{2\pi k'sd}{L}, \quad 0<k'<s \tag{5.3}$$

$$a_s = \frac{1}{2n} \sum_{s=0}^{2n-1} I(sd) \cos(s\pi) \tag{5.4}$$

and

$$b_{k'} = \frac{1}{n} \sum_{s=0}^{2n-1} I(sd) \sin\frac{2\pi k'sd}{L}, \quad 0<k'<s. \tag{5.5}$$

k is related to the frequency f in the beat pattern by $k = fL/v$, The Fourier coefficients are calculated with a WATFIV program which yields a plot of a_k versus f and the frequencies are given by the maxima. The criterion for the existence of such a frequency was that its peak height should be at least thrice the overall background. A polynomial interpolation was used to determine the precise value of the maxima.

To estimate the error in the frequency that arises from the statistical error in the intensity measurements, error bars were drawn on each point of the beat patterns in Figs. 11, 12, 13 and 14. The values assigned to the data entering the program for Fourier analysis were then taken to be alternatively the upper and lower limits of the error bar of neighboring points. In this manner it is found that the statistical error in the frequency measurements is below ±0.3%.

V.2 Fourier Transform of Quench Radiation

To compare the experimental frequencies with theory, the theoretical beat patterns are Fourier analyzed as well. Since in our experiments the radiation is observed parallel to the applied field, only the $I(\pi/2,0,t)$(Eq. 2.60) needs to be considered. The Fourier transform of $I(\pi/2,0,t)$ is proportional to

$$\int_0^\infty |A'(t)|^2 e^{i\omega t} dt \qquad (5.6)$$

Using equation (2.54) the previous expression becomes

$$F^2 \sum_{F,M,F'} \sum_{k,k'} \int_0^\infty e^{i(\beta_k^{(M)} - \beta_{k'}^{(M)} + \omega)t} \, \mathrm{Res}\{B_{F',M'}^{F,M}(\omega_1)\}_{\omega_1=\beta_k^{(M)}}$$

$$\times \mathrm{Res}\,\{B_{F',M'}^{F,M}(\omega_1)\}^*_{\omega_1=\beta_{k'}^{(M)}} \, dt \qquad (5.7)$$

The integrated result is

$$F^2 \sum_{F,M,F'} \sum_{k,k'} \frac{i}{\beta_k^{(M)} - \beta_{k'}^{(M)} + \omega} \, \mathrm{Res}\{B_{F',M'}^{F,M}(\omega_1)\}_{\omega_1=\beta_k^{(M)}}$$

$$\times \mathrm{Res}\{B_{F',M'}^{F,M}(\omega_1)\}^*_{\omega_1=\beta_{k'}^{(M)}} \qquad (5.8)$$

The physical significance of the Fourier transform will be more transparent if the following approximations are taken. To a first approximation, $-\beta_k^{(M)}$ and $-\beta_{k'}^{(M)}$ are approximately equal to $E_k=E_k^0-i\Gamma_k/2$ and $E_{k'}=E_{k'}^0-i\Gamma_{k'}/2$ respectively. For values of $\omega \approx E_k^0-E_{k'}^0$, typical terms in the $\cos\omega t$ and $\sin\omega t$ Fourier transforms are approximately given by

$$F_{kk'}^{(c)}(\omega) \approx \frac{\mathrm{Re}(a_k a_{k'}) \, \Gamma_{kk'}/2}{(E_k^0 - E_{k'}^0 - \omega)^2 + \Gamma_{kk'}^2/4} \qquad (5.9)$$

$$F^{(s)}_{kk'}(\omega) \simeq - \frac{\mathrm{Re}(a_k a_{k'})\,(E^o_k - E^o_{k'} - \omega)}{(E^o_k - E^o_{k'} - \omega)^2 + \Gamma^2_{kk'}/4} \qquad (5.10)$$

with

$$\Gamma_{kk'} = \Gamma_k - \Gamma_{k'}$$

and

$$a_k \simeq \mathrm{Res}\,\{B^{F,M}_{F',M'}(\omega_1)\}_{\omega_1 = E_k}$$

$$a_{k'} \simeq \mathrm{Res}\,\{B^{F,M}_{F',M'}(\omega_1)\}^*_{\omega_1 = E_{k'}}$$

(5.9) is more useful than (5.10) because it contains a peak at $\omega = E^o_k - E^o_{k'}$ with a Lorentzian line-shape, whereas $F^{(s)}_{kk'}$ vanishes at this frequency. The actual Fourier transform contains several overlapping peaks with some mixing of $F^{(c)}_{kk'}$ and $F^{(s)}_{kk'}$ shapes due to the imaginary parts of the coefficient a_k. However the cosine transform curve is still easier to interpret.

V.3 Comparison of Theory and Experiment

A comparison of theory and experiment is given in Table III. The calculated energy differences for the cross-terms contributing to the beat pattern are shown in column two. The peak positions in the theoretical and experimental cosine transforms are compared (column three and four). The

TABLE III.

Comparison of peak positions (in MHz) in the cosine Fourier transform of the theoretical and experimental time-dependent intensities

transition*	$\Delta E_{theo.}$	$(Peak)_{theo.}$	$(Peak)_{exp.}$
F = 83.5 V/cm			
(1): $2S_{1/2}$(00) - $2P_{1/2}$(10)	976	985	990±30
(2a): $2S_{1/2}$(11) - $2P_{1/2}$(11)	1142	1160	1150±30
(2b): $2S_{1/2}$(10) - $2P_{1/2}$(00)	1198		
F = 125 V/cm			
(1): $2S_{1/2}$(00) - $2P_{1/2}$(10)	1052	1063	990±30
(2a): $2S_{1/2}$(11) - $2P_{1/2}$(11)	1207	1227	1187±30
(2b): $2S_{1/2}$(10) - $2P_{1/2}$(00)	1259		
F = 167 V/cm			
(1): $2S_{1/2}$(00) - $2P_{1/2}$(10)	1150	1162	1127±30
(2a): $2S_{1/2}$(11) - $2P_{1/2}$(11)	1291	1314	1303±30
(2b): $2S_{1/2}$(10) - $2P_{1/2}$(00)	1340		
(3a): $2S_{1/2}$(11) - $2P_{3/2}$(11)	9768	9785	9740±150
(3b): $2S_{1/2}$(11) - $2P_{3/2}$(21)	9812		
(3c): $2S_{1/2}$(10) - $2P_{3/2}$(20)	9821		
(4): $2S_{1/2}$(00) - $2P_{3/2}$(10)	9950	10031	10134±150
(5a): $2P_{1/2}$(11) - $2P_{3/2}$(11)	11059	11072	11025±150
(5b): $2P_{1/2}$(10) - $2P_{3/2}$(10)	11100		
(5c): $2P_{1/2}$(11) - $2P_{3/2}$(21)	11103		
(5d): $2P_{1/2}$(00) - $2P_{3/2}$(20)	11161		

*The numbers in brackets denote the hyperfine quantum numbers (FM_F).

theoretical intensities include an allowance for instrumental broading. This, together with the above interference effects, accounts for the differences between $\Delta E_{theo.}$ and $(Peak)_{theo.}$ in the table. Many of the peaks are within a line width of each other and are therefore not resolvable in either the theoretical or experimental transforms. The five virtual transitions that have been resolved are shown in Fig. 16 where they are labelled in accordance with the notation of Table III. Since the quantization axis has been chosen parallel to the electric field direction only the $\Delta M_F = 0$ transitions are allowed.

For the low frequencies ($\sim 10^3$MHz), uncertainties in the field strength (~±2%), beam velocity (~±1%) and time origin for switching on the field, each contribute an uncertainty of about ±10HMz in the peak position relative to the theoretical value. The uncertainty arising from counting statistics is negligible (<1MHz). For the high frequencies ($\sim 10^4$MHz) the error is dominated by the beam velocity uncertainty (~±100MHz) with smaller contribution from the statistical uncertainty (~±30MHz) and time-origin uncertainty (~±20MHz). The maximum uncertainties quoted in Table III are thus about ±30MHz and ±150MHz, respectively. Except for the two results at F = 125 V/cm, all the peak positions agree within these error limits.

V.4 Conclusion

The only previous measurements of comparable accuracy are the beam-foil quantum beat results of Andrä (1970), and

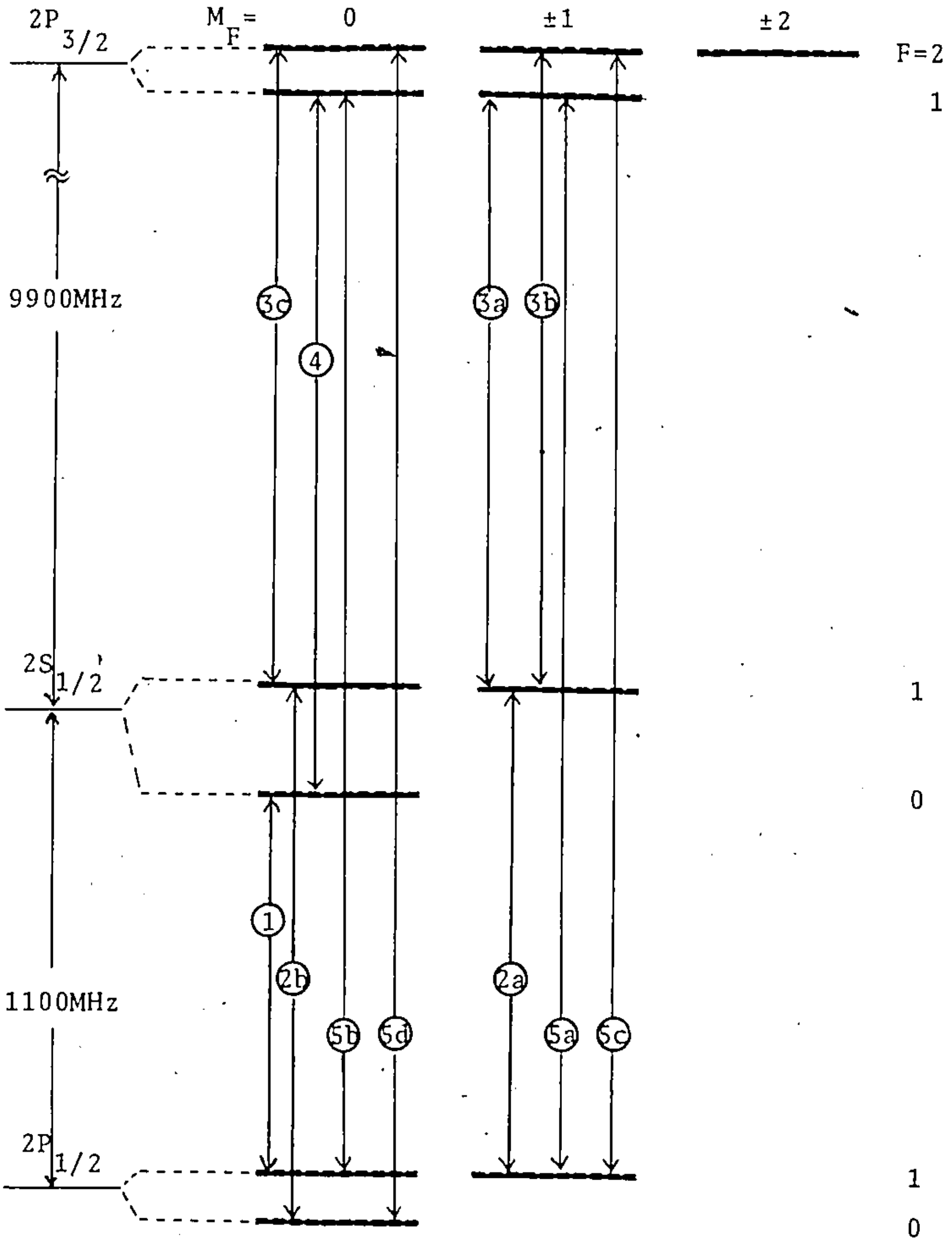

Fig. 16 Virtual transitions between hyperfine levels of the n=2 state of hydrogen relevant to the observed quantum beats. Labels correspond to those used in Table III.

the level crossing results of Kollath and Kleinpoppen (1974). We observe several additional frequencies and our results are the first to separate quantitatively some of the individual hyperfine structure contributions.

Furthermore we believe our experiment to be the first in which all three effects, the Lamb-shift oscillations (~1058MHz), the hyperfine structure modulation (~177MHz) and and the fine structure oscillations (~10969 HMz), have been observed simultaneously. This raises the interesting possibility of finding accurate values for frequency ratios from a single experiment for hydrogen and deuterium.

APPENDIX

OPTIMIZATION OF RESOLUTION

To detect high frequency quantum beats, high spatial resolution on the beam axis was required. To accomplish this, the two slits of the photon detection system (Fig. 4) were made very narrow (0.1mm) and given the same width. Since with Lyman-α photons $\lambda/d \sim 10^{-3}$ is small it was erroneously believed that diffraction effects could be neglected. However, after we found that a higher resolution could be obtained by opening the slits, it was realized that Fresnel diffraction was important, even for slit widths as large as 0.1mm.

To reduce the limitations resulting from the Fresnel diffraction we calculated the width ratio for slits S_1 and S_2 that would give optimum resolution. In Fig. 17 the radiating beam of atoms along the z axis is considered as a series of incoherent point sources. The sources are incoherent because the quenching process is of a statistical nature and the atoms radiate completely independently of each other. First we consider an arbitrary point source S on the beam axis and calculate the intensity at an arbitrary point P inside the opening of slit S_2. Light emitting from S makes an optical disturbance at an area element centered about point C inside slit S_1. This in turn generates an optical disturbance at point P. For small slit widths, when $SC+CP \simeq SP$, the optical disturbance at P can be written as (see, for example, Klein,

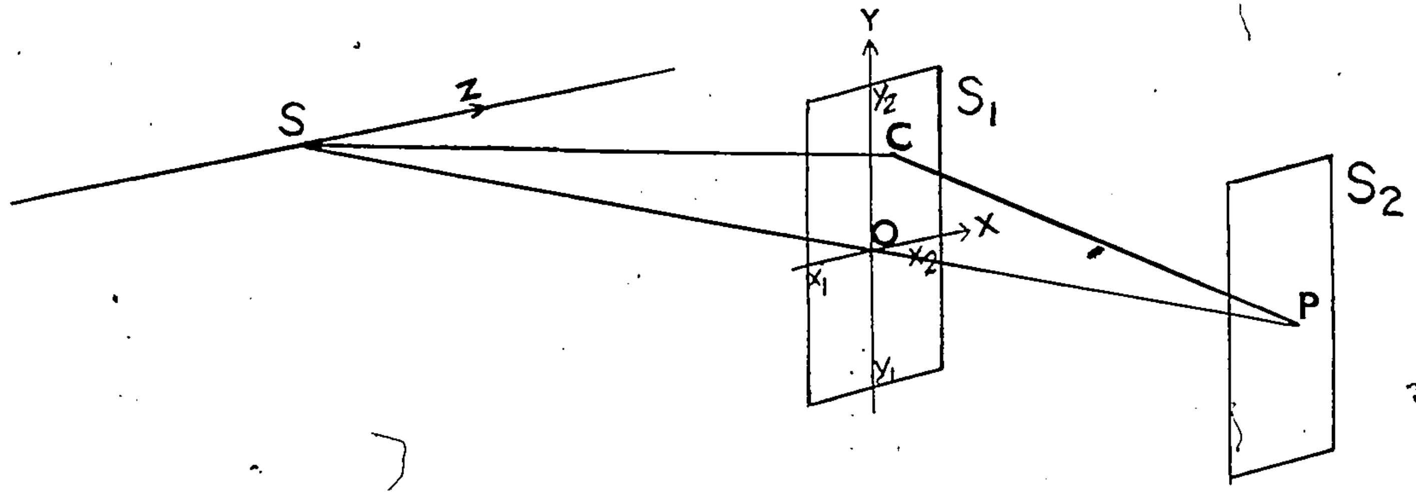

Fig. 17 Fresnel diffraction arising from a point source S on a line z for two rectangular slits S_1 and S_2.

1970)

$$E_p = \frac{iAe^{-ik|SP|}}{2|SP|}\int_{u_1}^{u_2} e^{i\pi u^2/2}du \int_{v_1}^{v_2} e^{i\pi v^2/2}dv$$

where A is the amplitude of the disturbance at the source S and u and v are related to the coordinates x and y, respectively, of the point C on the plane of the slit S_1 by

$$u = \sqrt{k/\pi r}\ x$$

$$v = \sqrt{k/\pi r}\ y$$

where

$$1/r = 1/SO + 1/PO.$$

Since the slits of our detection system are very long, the integral over v can be replaced by

$$\int_{-\infty}^{\infty} e^{i\pi v^2/2}dv = \sqrt{2}\ e^{i\pi/4}$$

and E_p becomes

$$E_p = \frac{1}{\sqrt{2}\ |SP|}Ae^{-i(k|SP|-3\pi/4)}\int_{u_1}^{u_2} e^{i\pi u^2/2}du$$

Thus the optical intensity at P arising from a point source S is given by

$$I_p = \frac{1}{2|SP|^2}A^2\{\{C(u_2) - C(u_1)\}^2 + \{S(u_2) - S(u_1)\}\}^2$$

where C(u) and S(u) are the Fresnel integrals given by

$$C(u) = \int_0^u \cos\ (\pi u^2/2)\ du$$

$$S(u) = \int_0^u \sin\ (\pi u^2/2)\ du$$

The total optical intensity from the point source at z arriving at slit S_2 is

$$I(z) = \int I_p dS_2$$

where the integration extends over the entire area of slit S_2.

Fig. 18 shows the z dependence of I(z) for various widths of slit S_2 for our optical system where S_1=0.20mm. The different curves have been calculated for point sources with the same brightness. The I-value at z=0 represents the intensity from a point source located at the viewing axis of the uv detector.

It can be noticed that the half-widths of the various curves are approximately the same. Because of this, the best spatial resolution on the beam axis is given by the curves that weigh the I-values near z=0 most heavily. This occurs for those curves that are most sharply peaked. We have chosen a value of S_2=0.15mm and have experimentally verified that S_2 values of 0.18mm and 0.12mm gave poorer resolution.

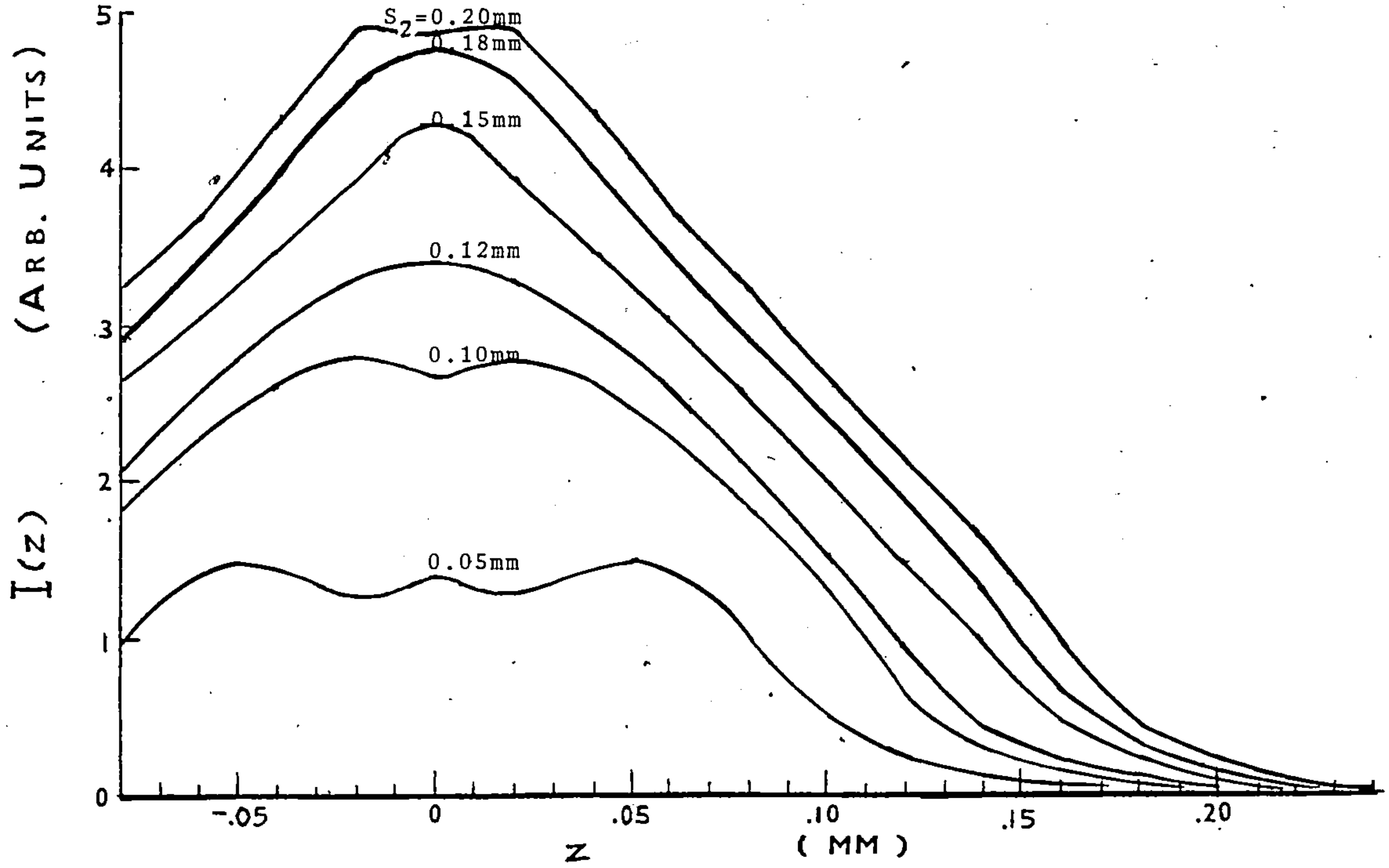

Fig. 18. The z dependence of I(2) for various values of slit width S_2 (see text).

REFERENCES

Alguard, M. J. and Drake, C. W. 1973. Phys. Rev. A8, 27.

Andrä, H. J. 1970. Phys. Rev. A2, 2200.

Andrä, H. J. 1974. Physica Scripta 9, 257.

Andrä, H. J., Dobberstein, P., Gaupp, A. and Wittmann. W. 1973. Nuclear Inst. and Methods 110, 301.

Baylis, W. E. Department of Physics, University of Windsor. Private communication.

Brodsky, S. J. and Parsons, R. G. 1967. Phys. Rev. 163, 134.

Cosens, B. L. and Vorburger, T. V. 1970. Phys. Rev. A2, 16.

Dahlberg, D. A., Anderson, D. K. and Dayton, I. E. 1968. Phys. Rev. 170, 127.

Drake, G. W. F., Victor, G. A. and Dalgarno A. 1969. Phys. Rev. 180, 25.

Drake, G. W. F. and Grimley, R. B. 1973. Phys. Rev. A8, 157.

Drake, G. W. F. and Grimley, R. B. 1975. Phys. Rev. A11, 1614.

Drake, G. W. F., Farago, P. S. and van Wijngaarden, A. 1975. Phys. Rev. A11, 1621.

Erickson, G. W. 1971. Phys. Rev. Lett. 27, 780.

Heberle, J. W., Reich, H. A. and Kusch, P. 1956. Phys. Rev. 101, 612.

Hicks, W. W., Hess, R. A. and Cooper, W. S. 1972. Phys. Rev. A5, 490.

Kaufman, S. L., Lamb, W. E., Lea, K. R. and Leventhal, M. 1971. Phys. Rev. A4, 2128.

Klein, M. V. 1970. Optics, p. 363, John Wiley, New York.

Kollath, K. J. and Kleinpoppen, H. 1974. Phys. Rev. A10, 1519.

Krotkov, R. V., Byron, F. W., Medeiros, J. A. and Yang, K. H. 1972. Phys. Rev. A5, 2078.

Lamb, W. E. and Retherford, R. C. 1947. Phys. Rev. 72, 241

Lindhard, J., Scharff, M. and Schiφtt, H. E. 1963. Kgl. Danske Videnskab. Selskab, Mat. Fys. Medd. 33, 14.

Lundeen, S. R. and Pinkin, F. M. 1975. Phys. Rev. Lett. 34, 1368.

Lundeen, S. R., Jossop, P. E. and Pinkin, F. M. 1975. Phys. Rev. Lett. 34, 377.

Mohr, P. J. 1975. Phys. Rev. Lett. 34, 1050.

Oppenheimer, J. R. 1928. Phys. Rev. 31, 349.

Robiscoe, R. T. and Shyn, T. W. 1970. Phys. Rev. Lett. 24, 559.

Shyn, T. W., Williams, W. L., Robiscoe, R. T. and Rebane, T. 1971. Phys. Rev. A3, 116.

VITA AUCTORIS

The author was born in Muar, Malaysia in May of 1943. He completed his high school education in 1960 and worked as a primary school teacher for the following two years. In 1963 he enrolled Nanyang University, Singapore and then obtained his B.Sc. degree in Physics in 1967. He joined a machinery distributor in Kuala Lumpur after he graduated.

In 1970 he was admitted to Lakehead University and received his M.Sc. degree after two years of study. In September 1972 he registered at The University of Windsor to work towards a Ph.D. degree in Physics.